

# Forced Atmospheric Teleconnections During 1979-2014

Tao Zhang<sup>1,2</sup>, Martin P. Hoerling<sup>2</sup>, Judith Perlwitz<sup>1,2</sup>, and Taiyi Xu<sup>1,2</sup>

<sup>1</sup>Cooperative Institute for Research in Environmental Sciences

University of Colorado

Boulder, Colorado

<sup>2</sup>NOAA Earth System Research Laboratory

Physical Sciences Division

Boulder, Colorado

*3<sup>rd</sup> Revised version*

*(Submitted to Journal of Climate)*

January 6, 2016

Corresponding author address:

Dr. Tao Zhang

NOAA/ESRL/PSD

325 Broadway, R/PSD1

Boulder, CO 80305

Email: [tao.zhang@noaa.gov](mailto:tao.zhang@noaa.gov)

## **Abstract**

Forced atmospheric teleconnections during 1979-2014 are examined using a 50-member ensemble of atmospheric general circulation model (AGCM) simulations subjected to observed variations in sea surface temperatures (SST), sea ice and carbon dioxide. Three primary modes of forced variability are identified using empirical orthogonal function (EOF) analysis of the ensemble mean wintertime extratropical Northern Hemisphere 500-hPa heights. The principal component time series of the first and second modes are highly correlated with Nino3.4 and Trans-Niño (TNI) SST indices, respectively, indicating mostly tropical sources. Their impacts are largely confined to the Pacific-North American (PNA) sector. The leading mode describes the canonical atmospheric teleconnection associated with El Niño-Southern Oscillation (ENSO) resembling the Tropical/Northern Hemisphere pattern. The second mode describes a wavetrain resembling the classic PNA pattern resulting from atmospheric sensitivity to ENSO asymmetry and from sensitivity to a tropical precursor SST for ENSO development.

The third mode is characterized by a hemisphere-scale increasing trend in heights. Based on a comparison with 50-member coupled climate simulations it is argued that this mode is strongly related to radiatively forced climate change, while the other two forced teleconnections are principally related to internal coupled ocean-atmosphere variability.

A trend in the leading forced mode is related to ENSO-like decadal variability and dominates the overall observed 500 hPa height trend since 1979. These model results indicate that the trend in the first mode is due to internal variability rather than external radiative forcings.

## 1. Introduction

A long-term topic of research specifically related to climate predictability on a regional scale is to improve our understanding of the sensitivity of atmospheric circulation patterns to forcings, either to surface boundary conditions related to SST variability, or to external radiative forcing (and its associated surface boundary changes). Since recent decades have experienced a substantial increase in anthropogenically caused radiative forcing (IPCC 2013), a question of particular interest is how such forcing has driven variations in atmospheric circulation patterns. The goal of this study is to examine the structure of forced atmospheric teleconnections during Northern Hemisphere (NH) wintertime since 1979 and explore the relative roles of natural variations and external forcings.

Atmospheric teleconnections are a backbone for North American seasonal climate predictability, especially related to the well-known El Niño-Southern Oscillation (ENSO) phenomenon (Horel and Wallace 1981; Trenberth et al. 1998). Posed in the context of seasonal climate prediction, the issue is whether different North American wintertime conditions during El Niños can be anticipated on the basis of particular characteristics of the SST forcing. To tackle the question of whether ENSO could be used as predictor for seasonal climate, but especially to assess the relevance of ENSO diversity (Capotondi et al. 2015), numerous groups have conducted atmospheric general circulation model (AGCM) experiments over the last 30 years. Early experiments produced conflicting results, with Geisler et al. (1985) finding a single geographically fixed pattern of NH response to different patterns and magnitudes of warm tropical Pacific SSTs, and Palmer

71 and Mansfield (1986b) finding the 1982-83 El Niño forcing to induce a different  
72 atmospheric response than that associated with composite El Niño forcing. A strong  
73 dependency of responses upon the quality of a model's climatology was shown to exist  
74 (e.g. Palmer and Mansfield 1986a), and early results using coarse resolution climate  
75 models, often performed in idealized perpetual January mode, need to be interpreted with  
76 great caution.

77  
78 A particular limitation that has plagued most modeling studies to date is the small  
79 ensemble sizes available from which to reliably extract the atmospheric responses for  
80 individual events. Thus, while Hoerling and Kumar (2000) found observed inter-El Niño  
81 variability in atmospheric circulation to be mostly unrelated to event-to-event differences  
82 in SSTs, the strength of their conclusion was undermined by their reliance on a relatively  
83 small 12-member ensemble. In a subsequent study, Hoerling and Kumar (2002)  
84 attempted to overcome the sampling problem by pooling simulations across four different  
85 models. The analysis of that multi-model ensemble revealed different response patterns  
86 depending on the characteristics of the tropical SST forcing, though much of the ENSO  
87 response manifested as a single spatial pattern. Whereas the larger ensemble size was  
88 evidently important for detecting additional atmospheric response patterns, the use of a  
89 multi-model approach introduced a new uncertainty in the interpretation. Recalling the  
90 lessons from early AGCM intercomparisons that revealed substantial model dependency  
91 in atmospheric responses, the possibility existed that the additional patterns found in  
92 Hoerling and Kumar (2002) were not signatures of a robust sensitivity. Furthermore,  
93 similar to the problem of potentially blurring sharper images of atmospheric responses to



94 ENSO when constructing an observed composite, the process of multi-model averaging  
95 may likewise obscure such patterns.

96  
97 To overcome these limitations, Kumar et al. (2005) diagnosed an 80-member ensemble of  
98 AGCM historical runs using a single model. Their approach took advantage of a lagged  
99 ensemble of hindcast experiments that were being routinely conducted as part of the  
100 National Centers for Environmental Prediction (NCEP) seasonal forecast system.  
101 Applying empirical orthogonal function (EOF) analysis to the ensemble mean as in  
102 Hoerling and Kumar (2002), they found a leading atmospheric response pattern bearing  
103 considerable resemblance to the ENSO teleconnection pattern determined by Horel and  
104 Wallace (1981), but importantly explaining only about half of the magnitude in overall  
105 wintertime SST forced variability. The second response pattern exhibited strong zonal  
106 symmetry, whose time series was a trend during the 1980-2000 period of study. A third  
107 pattern again revealed strong regional variability, resembling some features of the third  
108 EOF pattern in Hoerling and Kumar (2002).

109  
110 In sum, the two large ensemble model studies on SST-forced wintertime atmospheric  
111 circulations---one from a multi-model approach and a second from a particular model---  
112 indicate that a single teleconnection pattern resembling the ENSO composite determined  
113 by Horel and Wallace (1981) is indeed a robust and a dominant structure of the  
114 atmospheric circulation sensitivity to SST variability. To first-order, the magnitude and  
115 phase of this pattern can be understood to vary linearly with the magnitude and phase of  
116 ENSO-related tropical Pacific variations. This view of the atmospheric sensitivity

appears to account for roughly half of the wintertime NH variability in *SST forced circulation variability*, though a greater portion over select regions such as the central North Pacific. Higher-order patterns are less well understood, and currently lack clear physical interpretation. For instance, the third leading pattern has been argued to be linked to SST-driven teleconnections during non-ENSO years in Hoerling and Kumar (2002), while a similar pattern in Kumar et al. (2005) was believed to result from the nonlinear atmospheric response to extreme opposite phases of ENSO. Also unresolved is the physical explanation for a more zonally symmetric response pattern that appears to be emergent in the time series of the forced solutions.

In so far as prior analyses have ended in either 1999 or 2000, it is important to update the study to include a period in which external radiative forcing of climate has led to a detectable effects on sea surface temperatures (IPCC 2013), though effects on atmospheric circulation remain unclear. Further, it is important to understand whether the dominant ENSO-related teleconnection pattern has changed during this period of anthropogenic climate change.

This study addresses the nature and causes of boundary and externally forced modes of extratropical Northern Hemisphere circulation variability over the recent period (1979-2014) by utilizing large ensemble sized AGCM and coupled atmosphere-ocean model simulations. The model and analysis methods are described in Section 2. Section 3 then focuses on a physical interpretation of the December-February atmospheric sensitivity to SST variability for the period 1979-2014 using both observations and model data. To

identify the role of different physical processes, both observed SST forced Atmospheric GCM simulations and radiatively forced coupled ocean-atmospheric GCM simulations are intercompared. Section 4 summaries our physical understanding of the forced atmospheric teleconnections during 1979-2014.

## **2. Data and Methods**

### **a. Observed and model data**

The characteristics of atmospheric variability are diagnosed from analysis of 500 hPa geopotential height fields conducted over the region 20°N-90°N. The study is of the Northern Hemisphere (NH) December-January-February (DJF) winter season and focuses on the recent 1979-2014 period. Estimates of the observed variability are derived from the National Centers for Environmental Prediction (NCEP)–National Center for Atmospheric Research (NCAR) reanalysis product (*Kalnay et al.* 1996). Analysis using other reanalysis products (ERA-Interim, Dee et al. 2011) is found to yield very similar results.

In order to determine the physical factors responsible for the observed 500 hPa height variability, we utilize atmospheric models (also called Atmospheric Model Intercomparison Project (AMIP) experiments) and coupled ocean-atmospheric models (also called Coupled Model Intercomparison Project (CMIP) experiments). For the former, the study primarily uses the National Centers for Environmental Prediction (NCEP) Global Forecast System model version 2 (GFSv2), the atmospheric component of the Climate Forecast System (CFS) version 2 (*Saha et al.* 2014). The model is run at

T126 horizontal resolution with 64 vertical levels, and forced with specified observed monthly varying sea surface temperatures, sea ice (Hurrell et al. 2008), and carbon dioxide concentrations for 1979-2014. Climatological values are specified for other greenhouse gases (e.g. CH<sub>4</sub>, NO<sub>2</sub>, O<sub>3</sub>, CFCs), aerosols, solar, and volcanic aerosols. A 50-member ensemble is conducted, each member forced identically but differing only by its initial atmospheric condition. The time evolving forced signal is derived from analysis of the 50-member ensemble average. To assess the robustness of key features in the GFS forced responses, we also diagnosis the time evolving signal from an 85-member ensemble of the European Center-Hamburg Max Planck Institute for Meteorology model 4.5 (ECHAM4.5; Roeckner et al. 1996) that spans January 1950 through February 2003. The model was run at T42 horizontal resolution with 19 vertical levels.

The signal in these AMIP experiments is further diagnosed to assess the component linked to changes in external radiative forcing, which may affect variability in 500 hPa heights through its influence on lower boundary conditions such as SSTs and sea ice (e.g. related to the ocean's response to long term global warming) and through direct atmospheric effects of changes in radiative forcing. To isolate the role of the external radiative forcing alone, we use a multi-model, 50-member ensemble of historical CMIP simulations. A 20-member ensemble is based on the Community Climate System Model, version 4 (CCSM4; Gent et al. 2011) whose atmospheric component is Community Atmospheric Model version 4 (CAM4; Neale et al. 2010), and a 30-member ensemble (Kay et al. 2015) is based on the Community Earth System Model version 1 (CESM1; Meehl et al. 2013) whose atmospheric component is CAM5 (Neale et al. 2012). Both

atmospheric components are run at  $\sim 1^\circ$  horizontal resolution, with 26 vertical levels in CAM4 and 30 levels in CAM5. Each member of these two coupled model runs is similarly driven by changes in greenhouse gases, anthropogenic aerosols, solar and volcanic aerosols, with starting from different initial conditions. The radiatively forced atmospheric signals are derived from the ensemble-mean of 50 coupled runs, in order to effectively separate the atmospheric response pattern from those arising from unforced internal coupled ocean-atmospheric variability alone.

#### b. Diagnostic methods

The observed leading structures of the NH wintertime circulation patterns are obtained by applying empirical orthogonal function (EOF) analysis to DJF seasonally averaged 500-hPa heights for the 35 years of data during 1979-2014 period. The EOF analysis is based on the covariance matrix for  $20^\circ\text{N}$ - $90^\circ\text{N}$  latitude bands, and a latitudinal weighting prior to the EOF analysis is used. The EOF patterns are presented as regressions against the principal component (PC) time series. Note that unrotated EOFs utilized here are constructed to be both spatially and temporally uncorrelated to each other.

In this study, we determine the leading EOF modes of ensemble mean AMIP and CMIP data, which allows us to isolate the forced signals. By comparison, leading EOF modes of the observational record, or concatenated from individual ensemble members will involve unforced internal atmospheric (or coupled ocean-atmospheric) variability.

In Appendix A, we provide a comparison of the patterns of the observed and GFS simulated first three leading modes of variability of DJF 500 hPa geopotential heights. This comparison demonstrates that the model is capable of capturing the observed two leading modes of variability when concatenating the individual members of the GFS AMIP simulations. These modes can also be largely reproduced in a long climatological run driven with climatological lower boundary conditions, suggesting that the internal atmospheric variability may play a dominant role in Northern Hemisphere wintertime height variability. Section 3 will present the analysis of the fraction of the forced atmospheric variability versus the total wintertime height variability to further quantify the role of internal atmospheric variability.

As mentioned above, EOFs are calculated of the ensemble mean 500 hPa heights of the AMIP and the CMIP data. For the AMIP model suite, the resulting patterns are of the atmospheric sensitivity to the specified SST, sea ice, and radiatively forcing during 1979-2014. These forcings commingle both internal ocean variations (e.g., ENSO) and external variations related to anthropogenic climate change. For the CMIP model suite, the resulting patterns are of the atmospheric sensitivity to specified radiative forcing alone. While the coupled models produce internal ocean variations such as ENSO, these are not temporally coherent among the individual ensemble members in the manner that they are (by specification) in AMIP experiments. Thus, any SST-forced component of height variability in the CMIP analysis will be principally related to the trend component of global SST change that is coherent with the time series of radiative forcing.

We also carry out a composite analysis for extreme phases of the EOF patterns and determine the associated anomaly patterns of 500-hPa heights, sea surface temperatures, and North American surface temperature and precipitation.

### 3. Results

#### *a. Principal time-varying forced signals*

Figure 1 shows wintertime (DJF) 500 hPa height structures based on the two leading EOFs of the ensemble-averaged AMIP simulations. Together these explain 79% of the total boundary forced height variance. Contours in the left panels are the ensemble-mean 500 hPa heights regressed against each eigenvector's PC time series shown in the right panels for 1979-2014.

A wave train having principal centers over the Pacific-North American sector describes the height pattern maximizing variance in the extratropical NH forced solutions. Its structure is well-known, resembling the observed height anomalies that are linearly related to Nino3.4 SST variability (see Figure 3). This anomaly pattern, also called the Tropical/Northern Hemisphere (TNH) pattern (Mo and Livezey, 1986), resembles the configuration related to the leading EOFs of wintertime heights in observations (see Figure A1). The time series for this leading mode shows clear co-variability with ENSO, having positive polarity (i.e., the phase as shown in Fig. 1) during warm events (e.g. 1982/83, 1991/92, 1997/98, 2002/03, 2009/10) and negative polarity (i.e., the opposite phase to that shown in Fig. 1) during cold events (e.g. 1988/89, 1998/99, 1999/2000,

2007/08, 2011/12). This pattern alone explains 56% of total boundary forced component of extratropical NH wintertime height variability.

The height pattern associated with the second mode of forced AMIP solutions also describes a wavetrain, but resembles the classic PNA pattern. Explaining 23% of the total boundary forced height variability over the NH extratropics, its centers-of-action are in spatial quadrature with the leading forced solution. Hartmann (2015) found a similar mode of height variability by regressing winter 500 hPa heights onto the PC time series of the second EOF of global 1979-2014 SST. This pattern arises from several configurations of tropical Pacific SST variability. During strong El Niño events, both PC1 and PC2 have large values, with the second EOF pattern acting to modify the overall forced response by effectively shifting the centers-of-action of the first EOF pattern eastward. In this sense, various magnitudes of PC1 and PC2 during warm events describe so-called “flavors of El Niño” (e.g. Trenberth 1993; Hoerling and Kumar 2002; Capotondi et al. 2015). The second EOF also describes the asymmetry in teleconnections between El Niño and La Niña events, and is thus the spatial manifestation of the nonlinearity in atmosphere responses to ENSO’s opposite phases. Finally, this pattern can arise in the absence of ENSO, being the dominant forced solution at times when NINO3.4 SSTs are “ENSO-neutral”. Thus, while the stronger amplitudes in the corresponding PC-2 time series (Fig. 1, lower right) tend to occur during ENSO events (e.g. 1982/83, 1991/92, 1997/98 warm events, and 1988/89, 1998/99, 2007/08, 2010/11, 2011/12 cold events), large projections also occur during several ENSO-neutral years (1985/86, 1996/97, 2001/02, 2013/14). At such times, the forced solution is materially



different from the canonical ENSO teleconnection and has different impacts on North American surface temperature and precipitation than the canonical ENSO signals, as described further in section 3b.

We have utilized the large ensemble AMIP simulation from a different atmospheric circulation model to repeat the analysis and found that the results in Figure 1 are robust (Appendix B). This intercomparison indicates that the atmospheric sensitivities are unique to the nature of the boundary forcing to which each atmospheric model was subjected, rather than depending on the selection of a particular model. Our subsequent analysis is thus based on the GFS data.

We diagnose the scatter relationship between the PC indices shown in Figure 1 and various tropical Pacific SST indices to better understand the linkage between the first two EOF modes and oceanic forcing during 1979-2014. The top panel of Fig. 2 shows the relationship between the Nino3.4 standardized SST index, which is commonly used to monitor ENSO, and the PC time series for the EOF1 500 hPa height mode (PC1). The bottom panel of Fig. 2 shows the relationship between the Trans-Niño standardized SST index (TNI), which measures the contrast in SSTs across the equatorial Pacific and helps to capture the evolution of ENSO during its transition period (Trenberth and Stepaniak 2001), and the PC time series for the EOF2 500 hPa height mode (PC2). The correlation between PC1 and Nino3.4 indices is 0.90, confirming that the height pattern associated with the leading mode of forced AMIP solutions is the atmospheric expression of ENSO forcing; the so-called canonical ENSO teleconnection. The correlation between PC2

index and TNI index is also high (0.74), indicating that the height pattern associated with the second mode of forced AMIP solutions is linked to the evolution of ENSO.

To further confirm the linkage between the PC indices and tropical Pacific SST indices, we have regressed the wintertime 500 hPa height from observations and the ensemble-averaged AMIP simulations onto the Nino3.4 variability and the TNI index, respectively (Figure 3). The results show that the model reproduces well the observed atmospheric circulations associated with each ocean forcing. The similarities between the patterns in Figure 3 and Figure 1 demonstrate that the height patterns associated with the first two modes of forced AMIP solutions represent tropical SST forced teleconnections.

Whereas the overall temporal correlation between the PC1 and PC2 time series is zero, there is nonetheless a strong physical relationship between these two as mentioned previously. To explore the connection between the PC1 index and PC2 index, Figure 4 shows the scatter relationship between them. While there is no linear correlation between these two PC time series by statistical construct, a nonlinear relationship is evident. For the extremes values of PC1, PC2 is always positive. Further, the extreme positive occurrences of PC2 arise solely in concert with strong PC1 states. Recalling that the latter is a proxy for NINO3.4 SST variability, this result illustrates the nonlinearity of atmospheric teleconnections through which the second response pattern is of the same phase during both strong El Niño and La Niña events. This non-linear relation between the PC1 and PC2 circulation patterns is mirrored by a similar non-linear relation between the two leading EOF modes of tropical Pacific SSTs (Dommenget et al. 2013), with those

SST patterns being well described by the NINO3.4 and TNI indices, respectively. Affirmed hereby is that the difference between the oceanic expressions of El Niño and La Niña events is responsible for a difference in atmospheric teleconnections between ENSO's extreme states.

An interesting feature of the scatter relation is that the strong negative phases of PC2 occur almost exclusively when PC1 is near-normal, namely only during ENSO-neutral conditions during 1979-2014. It is unclear whether this is also true for the forced atmospheric teleconnections for other periods before 1979. Nonetheless, the result isolates the existence of a forced atmospheric teleconnection that is distinct from the well-known teleconnection occurring during mature ENSO conditions. The forced atmospheric circulation described by this PC2 is thus not a mere modifier of the canonical ENSO patterns, but can also exist as a unique stand-alone sensitivity pattern given particular states of the tropical ocean. As will be subsequently shown in composite analyses, this wintertime teleconnection emerges in the interlude between tropical SST evolutions from a recently completed La Niña to a subsequent El Niño. Within this transition toward El Niño, warm SSTs are often present in the tropical west Pacific and cool conditions are lingering in the tropical east Pacific, a pattern resembling the optimal structure for El Niño development 6-9 month later (Penland and Sardeshmukh 1995). These results indicate that there is a distinct atmospheric teleconnection (the negative phase of PC2) that accompanies such a precursor state to El Niño development.

#### *b. Composite forced signals*

Various characteristics of wintertime global climate associated with the leading forced atmospheric teleconnection are illustrated in Fig. 5. Shown are the composite patterns of Northern Hemisphere 500-hPa height, tropical SST and precipitation, North American surface temperature, and North American precipitation based on the upper and lower quintile of the PC1 time series during 1979-2014. Each composite consists of a wintertime average constructed from the 7 strongest cases averaged across the 50-member model simulation.

For positive PC1 (Fig. 5, left), tropospheric circulation anomalies (top panel) resemble the Tropical/Northern Hemisphere (TNH) pattern (Mo and Livezey 1986). This positive phase occurs in concert with warm equatorial Pacific SSTs during the mature phase of El Niño (second panel). The well-known southeastward shift of low pressure from the Aleutians into the Gulf of Alaska and a development of anomalously high pressure over central Canada are part of a hemispheric wave train that brings above-normal temperatures to central and eastern North America (third panel) and above-normal rainfall to the southwestern United States (bottom panel). For negative PC1 values (Fig. 5, right), the global climate conditions are almost a mirror image, affirming the dominant linearity in atmospheric response to the extreme values of the Nino3.4 index. Some asymmetries are evident, however. For instance, the 500 hPa height anomaly centers are shifted 20-30° longitude west in the PC1 negative composite compared to PC1 positive composite, and resemble the Pacific-North American circulation pattern (Barnston and Livezey 1987) rather than the TNH pattern. Such asymmetry in the model's response is

consistent with observational evidence of nonlinearity in atmospheric teleconnections associated with El Niño and La Niña (e.g. Hoerling et al. 1997).

The asymmetry in global climate conditions between extreme phases of PC1 is diagnosed in Fig. 6, which presents the sum of composite anomalies for extreme positive PC1 (left panels, Figure 5) and negative PC1 (right panels, Figure 5). The asymmetric height pattern (top) is symptomatic of the aforementioned phase shift in teleconnections, a structure very similar to the second EOF pattern of forced atmospheric teleconnections (see Fig. 1). Consistent with the scatter relation of PC1 and PC2 time series, this result again demonstrates a physical relationship between the two leading EOFs of forced circulation, even though their respective time series are uncorrelated.

It is principally the difference in tropical forcing distinguishing strong El Niño from strong La Niña events that causes the asymmetry in teleconnections related to PC1 (e.g. Hoerling et al. 2001). Strong El Niños acquire larger SST amplitudes in the eastern equatorial Pacific whereas strong La Niñas acquire larger SST amplitudes in the western equatorial Pacific (Dommenget et al. 2013), the signature of which is captured in Fig. 6 (second panel). The resulting positive skew in the Nino3 index is further indication for nonlinearity in SST forcing (Burgers and Stephenson 1999; An and Jin 2004; Zhang et al. 2009; Zhang and Sun 2014), which could be mainly caused by the extraordinary 1982-83 and 1997-98 El Niño events (Takahashi et al. 2011). Tropical convection is sensitive to such differences, with strong El Niños exhibiting more enhanced rainfall in the eastern Pacific, whereas strong La Niñas have less enhanced rainfall in the western Pacific. As

will be subsequently shown, this dipole in tropical forcing is not solely a residual of ENSO variance, but also arises during non-ENSO winters when the tropics can likewise act to force a teleconnection pattern resembling EOF2.

The asymmetric component of US climate conditions is physically consistent with those expected from the circulation asymmetry, the physical linkages of which have been examined in detail in Zhang et al. (2014). Here we add the interpretation that the skew in ENSO SST distributions implants a tendency toward non-Gaussian statistics in North American surface temperature. Over eastern North America especially, an outcome of asymmetry in the tropically forced teleconnection is that warm conditions, which appear during both strong El Niño and La Niña, would occur with greater frequency than expected from assumptions of normality (see Fig. 6, third panel). The asymmetric component of precipitation (Fig. 6, bottom) has a somewhat different interpretation. The widespread wet conditions over the West Coast result from the fact that the strong El Niño wet signal in central-northern California is appreciably more intense than the La Niña dry signal. Further, strong El Niños do not yield substantial wintertime dryness over Oregon/Washington, whereas those areas are considerably wet during La Niña. Overall, these indications for asymmetry in US climate impacts, originating from teleconnections driven by ENSO extremes, reveal a rectified effect comprised of a wetter far western North America and a warmer eastern North America, than would prevail in a climate lacking extreme ENSO variability.

Figure 7 presents the various characteristics of wintertime global climate associated with the second EOF of forced atmospheric teleconnection. Noteworthy here is that the composite maps for positive PC2 (left panels) are virtually identical to those associated with the asymmetric component of PC1 (cf. Figure 6). This follows directly from the scatter relation of the two PC time series (Fig. 4) where it was shown that most of the extreme positive states of PC2 occur in concert with the extreme PC1 positive and negative states. Thus, the simulation years comprising the composite of 7 extreme positive PC2 events, used to construct the left panels in Fig. 7, consist of a sum of extreme positive and negative PC1 cases from which the results of Fig. 6 were constructed. Physically, this positive PC2 phase and its associated global climate conditions are principally linked to ENSO.

On the other hand, the composite maps for negative PC2 (Fig. 7, right panels) are identified with SST forcing that is distinct from the mature states of ENSO. This phase of the teleconnection, consisting of anomalous low pressure over the central Pacific and anomalous high pressure along western North America, occurs in association with warm equatorial SST anomalies located slightly west of the Dateline, and cold SST anomalies along the equatorial east Pacific. The structure and phase of this teleconnection can be physically understood as resulting from tropospheric wave driving by enhanced convection initiated over the warm waters of the western Pacific, as demonstrated in dynamical model studies (e.g. Ting and Sardeshmukh 1993) and in idealized SST-driven climate simulations (Hoerling and Kumar 2002). The SST pattern is analogous to a pattern that is the precursor to El Niño development (e.g. Penland and Sardeshmukh,

1995). The principal North American impact of this SST pattern is dry/warm across the western United States. Vimont et al. (2001, 2003a,b) and Alexander et al. (2010) provided a physical mechanism, the so called “seasonal footprinting mechanism” (SFM) for such a precursor mode to induce El Niño, by which North Pacific atmospheric variability during the preceding winter affects tropical Pacific SST anomaly and the development of ENSO in the following year.

An application of this result concerning PC2 is that it clarifies and supports recent interpretations on causes for California drought in 2013-14, in particular the possible role of tropical forcing (e.g. Wang et al. 2014; Seager et al, 2014). We note that the largest negative PC2 loading since 1979 occurred during the 2013-14 winter (see Fig. 1) indicating that this non-ENSO, tropically forced teleconnection was a candidate mechanism in the severe drought and heat over California and the Far West. The results of AMIP simulations using 7 different climate models also have found a wave pattern of the type described by this negative phase of PC2 during winter 2013-14 (Seager et al. 2014)

### *c. Radiatively forced time-varying atmospheric signals and trends*

Results in the previous sections indicate that the two leading forced teleconnections are strongly linked to interannual states of tropical Pacific SST forcing, either mature ENSO conditions or pre-cursor conditions preceding El Niño development. The PC1 time series also exhibits a downward trend during 1979-2014 (see Fig. 1), which may reflect an increased frequency of cold ENSO states in the recent decade compared to the first



decade, or may be suggestive of other low frequency forcing. The question arises in particular whether the trend in this leading teleconnection during 1979-2014, or trends in other manifestations of the model's forced responses, is symptomatic of atmospheric sensitivity to time variations in external radiative forcing.

To address this question, we begin by diagnosing the third EOF of the AMIP ensemble mean 500 hPa wintertime height variability (Fig. 8, top left). While explaining only 6% of the variance in forced height variability (the first two EOFs explain 80% of the variance), its pattern and temporal variability suggests a plausible physical interpretation in a framework of global warming. First, EOF3 primarily describes a monopole structure over the NH as a whole, a hemisphere-wide pattern distinct from the regional wave structures of EOF1 and EOF2 that were each confined to the Pacific-North American sector. Second, the PC3 time series (Fig. 8, top right) has a distinct upward trend that describes a tendency for NH heights to rise since 1979 as would be expected from the effects of anthropogenic greenhouse gas forcing.

The pattern of the third EOF and its temporal trend of the PC alone are however not sufficient for a physical interpretation related to climate change because this higher mode of variability is constrained by temporal and spatial orthogonality in relation to the leading two modes. Therefore, we utilize a 50-member ensemble of CMIP simulations. Recall that the only forcing that is temporally synchronized among every CMIP model realization is anthropogenic greenhouse gases, anthropogenic aerosols, solar and volcanic variability. The CMIP EOF1 regression pattern and the related PC are shown in the

bottom panels of Fig. 8. The leading 500 hPa height pattern associated with such forcing describes a hemisphere-wide monopole whose time series consists of an upward trend. These characteristics reproduce many features of the space-time variability of EOF3 from the AMIP analysis, including also the magnitude of variations, which are typically about 5 meters in both. Specifically, the CMIP EOF1 has a strong spatial congruence ( $r=0.79$ ) with the EOF3 of the AMIP model. By comparison, there is no appreciable spatial agreement of the externally forced solution with the EOF1 and EOF2 of the AMIP model ( $r=0.40$  and  $r=0.03$ , respectively). We also compared the root mean square (RMS) of the magnitude of three EOF patterns from AMIP analysis with that of EOF1 pattern from CMIP simulations. The results show that compared to EOF1 and EOF2 modes, the magnitude of EOF3 pattern from AMIP analysis is much closer to that of EOF1 pattern of CMIP simulations. The results, from several lines of evidence, thus indicate radiative forcing to be instrumental in understanding the third EOF of AMIP responses.

Considering the trend in the leading EOF of the AMIP response, our interpretation is that this is unlikely a symptom of sensitivity to time variations in external radiative forcing. We have calculated the ensemble mean of the leading EOFs derived from the individual historical coupled simulations (See Appendix C). The ensemble mean pattern is spatially similar to the leading EOF (EOF1) of the AMIP response (and also EOF1 of observed), and captures the dominant structure of the ENSO teleconnection (see Fig. C1, top left). However, unlike the time series of the AMIP EOF1, the time series of the EOF1 of the average of individual coupled runs exhibits no appreciable trend (Fig. C1, top right).

These results indicate that external radiative forcing has no significant effect on the trend in the leading ENSO teleconnection pattern, in the models studied herein.

We also note that the time series of EOF1 derived from individual coupled model samples can have a strong positive (or negative) trend, the magnitude of which was found to be at least as large as the trend in the AMIP EOF1 (Fig. C1, bottom right). There is thus a large range of internal variability on multi-decadal time scales in the coupled models. This result, together with the evidence that the leading ENSO teleconnection is not materially affected by external radiative forcing during 1979-2014, supports an interpretation that the trend in the forced ENSO teleconnection of AMIP response has resulted principally from internal coupled variability. We can not exclude the possibility that ENSO itself may be changing in response to external forcing, although CMIP model simulations do not show consensus on the response of ENSO variability to climate change (Guilyardi 2006; Collins et al. 2010; Stevenson 2012; Kim et al. 2014). Furthermore, long coupled runs for pre-industrial conditions yield decadal to centennial modulations of ENSO (Wittenberg, 2009; Yeh et al. 2011), and thus one would expect corresponding multi-decadal variations in forced atmospheric teleconnections. Due to the high correlation between AMIP PC1 time series and a N3.4 index, it is quite plausible that the trend in AMIP EOF1 is symptomatic of such internal ENSO-like multi-decadal variability.

How large is the contribution of radiative forcing changes to the total circulation variability during 1979-2014? To address this question, Figure 9 presents the ratio of

wintertime 500 hPa height variances calculated for the AMIP (top) and CMIP (bottom) simulations. The total variance, which appears in the denominator of the ratio, commingles forced variations and internally driven variations (either of the atmosphere alone in AMIP or of the coupled ocean-atmosphere in CMIP). Its magnitude and spatial pattern is very similar in the two model configurations (not shown). The forced components, which appear in the numerator of the ratio, are very different however. The forced component in CMIP represents the physical effects of external radiative forcing arising from both the atmosphere's sensitivity to lower boundary changes (e.g., a broad oceanic warming in response to increasing radiative forcing), and the direct effects of radiative forcing on the atmosphere alone. As shown in the lower panels of Fig. 9, this forced component is a small fraction of total variability, generally less than 5% poleward of 30°N. A similar pattern of variance ratios is found when using the AMIP EOF3 forced signal in the numerator (Figure 10), thus providing further evidence that radiative forcing is unlikely to be a substantial factor in driving year-to-year variability of wintertime extratropical circulation.

The results support the interpretation that radiative forcing has limited explanatory power for height variations during 1979-2014. As a consequence, knowledge of the time series of radiative forcing offers little potential for predicting the overall interannual variability in wintertime atmospheric circulation.

By contrast, the forced component in AMIP incorporates the atmosphere's sensitivity to the particular history of observed ocean variability, including especially ENSO variations

observed during 1979-2014, in addition to the aforementioned physical effects related to radiative forcing. Strong atmospheric forcing by the particular history of SST variations explains why the ratio of variances in the AMIP simulation, shown in the upper panels of Fig. 9, is much larger than in CMIP. The magnitude is nearly an order of magnitude greater in portions of the Pacific-North American region in AMIP versus CMIP. It is in that region especially where atmospheric responses to observed tropical Pacific SST variations that occurred during 1979-2014 dominates the overall boundary forced variance in AMIP.

The results of the AMIP analysis thus indicate the particular history of tropical Pacific SST variability to be key for understanding the nature of forced atmospheric teleconnections during 1979-2014. These SST forcings render appreciable explanatory power for PNA-sector height variations, and knowledge of the time series of ENSO and related internal states of the tropical Pacific Ocean offers substantial potential atmospheric predictability, whereas the radiative forcing alone explains little variance. The same distinction does not hold elsewhere. Both AMIP and CMIP variance ratios are small over the North Atlantic, Europe, and Asia. In those regions, the results of Fig. 9 indicate that neither radiative forcing alone, nor the additional knowledge of the sequence of observed SST variations, contributes appreciably to circulation variability thereby limiting overall interannual predictability.

Figure 11 reveals that it is principally EOF1, and not EOF3, that explains most of wintertime NH 500 hPa height trend occurring in the AMIP ensemble. The left panels of

Fig. 11 compare the 1979-2014 trend in 500 hPa heights associated with EOF1 (top) to the total AMIP ensemble mean trend (bottom). These are almost indistinguishable in pattern and magnitude indicating that irregularity in Nino3.4 SST variability during this period, with greater frequency of La Niña events in later years, is mainly responsible for trend in forced circulations. Incorporating the trend contribution from EOF3 doesn't materially change the trend derived from EOF1 alone (see Fig 11, top right). Most of the regional patterns of NH wintertime height change since 1979 thus appear unrelated to the radiative forcing time series, consistent with the findings of Perlwitz et al. (2015). We note, however, that the possibility can not be excluded that the CMIP models have biases relevant to this interpretation. In particular, a post-1979 trend toward cold states of the tropical eastern Pacific is a very low probability of CMIP models (e.g. Hoerling et al. 2010), which could indicate a different sensitivity to radiative forcing in nature in addition to the more likely possibility that this has been an extreme case of internal variability.

It is instructive to compare the AMIP ensemble mean height change since 1979 with the observed height change pattern. Agreement is strong, principally over the North Pacific where both indicate trends toward increased anticyclonic circulation (compare bottom panels of Fig. 11). The agreement over the North Pacific is not surprising given the high signal-to-noise ratio for interannual variability found in the AMIP simulations (Fig. 9). Physically, this observed trend toward anticyclonic circulation is consistent with atmospheric sensitivity to a change in ENSO statistics, with La Niña events more common during 1999-2014 while El Niños dominated the 1980s and 1990s. The ratio of

variance indicates that detectability of such a North Pacific circulation change in observations is expected to be high, and thus the fidelity of the simulated trend is not surprising. The interpretation is not particularly dependent on whether one interprets the change in Pacific basin SSTs during 1979-2014 as symptomatic of ENSO-like interdecadal variability (e.g. Zhang et al. 1997), or indicative of a Pacific decadal climate oscillation (e.g. Mantua et al. 1997). By contrast, an observed circulation trend over the North Atlantic basin, which projects onto a negative phase of the North Atlantic Oscillation (NAO), is not reconcilable with forcing in the AMIP (or CMIP) simulations. Here the ratio of variances analysis showed forcing to be ineffective in driving interannual variability of atmospheric circulation, and it is plausible that the recent trend toward the negative NAO phase is largely a symptom of internal atmospheric variability (see also Perlwitz et al. 2015).

#### **4. Summary and discussion**

In this study, the forced modes of NH winter 500-hPa heights for the period of 1979 to 2014 were determined by utilizing a 50-member ensemble of atmospheric general circulation model (GFSv2) simulations and by carrying out an EOF decomposition of the ensemble mean 500-hPa height anomalies. We identified three main modes that together explain about 85% of the forced variability of 500 hPa wintertime height variability poleward of 20°N.

The first two leading modes, which together explain 79% of the forced height variance, are associated with tropical SST forcing. The first EOF describes the canonical tropical-extratropical teleconnection pattern (TNH) that has historically been interpreted as the linear response to ENSO's extreme opposite phases. That is, the positive (negative) phase (indicated by PC values) of the first EOF mode is linked to the response during warm (cold) ENSO events. A high correlation ( $\sim 0.9$ ) between the principal component of this EOF and the Nino3.4 index therefore exists. The second forced mode describes the classic PNA circulation pattern, and is closely linked to the Trans-Nino index—a correlation coefficient of 0.74 is found between the TNI and the principal component time series of this mode.

Our analysis of the scatter relationship between the PCs of these first and second AMIP modes, together with composite analyses, offers new insights into the physics of this second forced teleconnection pattern. Its positive phase is shown to be an expression of the asymmetry in ENSO teleconnections between their extreme opposite warm and cold phases. This arises most strongly during the intense El Niño events of 1982/83 and 1997/98. Consistent with this asymmetry in ENSO teleconnections, we demonstrate that wet conditions occur over far western North America and warm conditions over eastern North America during both strong ENSO phases. Its negative phase is shown to be an expression of atmospheric responses that occur mostly during ENSO-neutral winters when a distinctive tropical SST pattern having warmth in the far western Pacific and coolness in the far eastern Pacific can arise. This forcing resembles a precursor state that often is followed by a mature El Niño event in 6-9 months. The principal climate impact



related to this forced teleconnection is an anomalously dry and warm climate across the western United States.

It should be noted that these two leading teleconnection modes are not particularly dependent upon just two strong warming events (1982/1983 El Niño and 1997/1998 El Niño) or the 1979-2014 period. We have recalculated the AMIP EOFs of 500 hPa heights by considering two separate periods (1984-1997 and 1999-2014), neither of which includes these two strong events. The two leading EOFs emerge with little change in structure in these sub-periods, with the principal difference being a reduced explained variance of EOF2. Based on the available ECHAM4.5 simulations spanning 1950-2003, we have compared the leading two EOF patterns of that model's forced teleconnections during 1950-1978 to the subsequent period, and found little appreciable difference. In light of the high consistency in the first two EOFs among models and for different periods of analysis, it is suggested that our analysis of the 1979-2014 period is robust and is likely representative of a longer period of study.

By comparing the AMIP (GFSv2) EOF analysis results with CMIP (CCSM4 and CESM1) EOF analysis we argue that the third AMIP EOF mode is associated with radiatively forced climate change. This mode explains 6% of the forced variance in the AMIP ensemble mean and is thus much weaker than the contribution from the first two modes. The time series of this third EOF consists mostly of a trend pattern that primarily describes increasing geopotential heights in the Northern Hemisphere, consistent with a global warming signal. However, a trend in the PC time series of AMIP EOF1 is found to

dominate the overall trend in the AMIP ensemble mean and observations during 1979-2014. Our analysis therefore suggests that the observed trend of winter heights during the recent period is more determined by the decadal variability associated with low frequency fluctuations in ENSO than by the external radiative forcing.

Our results have some relevance to the question of the atmospheric sensitivity to different “Faces of El Niño” (e.g. Capotondi et al. 2015). Studies have shown that, distinct from the canonical El Niño with warming in the eastern equatorial Pacific ocean (EP- El Niño), a different expression of SST warming confined to the central Pacific region also occurs. This latter warming pattern is referred to variously as the central Pacific (CP) El Niño (Yu and Kao 2007; Kao and Yu 2009), Date Line El Niño (Larkin and Harrison 2005), El Niño Modoki (Ashok et al. 2007), or warm pool El Niño (Kug et al. 2009). The central Pacific events have been interpreted as a nonlinear manifestation of the canonical ENSO (Takahashi et al. 2011; Dommenges et al. 2013; Johnson 2013). The question has been explored whether these two types of El Niño have different impacts on wintertime extratropical climate (e.g. Yeh et al. 2009; Yu et al. 2012). Our analysis indicates that there indeed exist additional forced atmospheric response patterns beyond a single canonical (linear) ENSO response, though the EOF approach is not suitable to clarifying the different structures of atmospheric responses across a continuous spectrum of El Niño warming patterns. A better understanding of these different structures is a subject of ongoing research.

Future work is also needed to better understand the predictive value implicit in the knowledge of these forced teleconnections for US climate. For instance, is the potential predictability implied by the three leading teleconnections being realized in current climate prediction systems? What is the contribution of the different modes to US seasonal forecast skill? And, at what lead times are the different forcings of these teleconnections themselves predictable?

The PC time series of the forced teleconnections describe distinct “forecasts of opportunity”. Some are well known, such as the strong El Niño events in 1982-83 and 1997-98. Others are less well known, and deserving additional study. For example, during winter of 2013-14 the negative phase of the second mode was strongly enhanced, an important indicator for a possible role of tropical forcing in that winter and its impact on California precipitation deficits and high temperatures during that winter (see also Seager et al. 2014). Hartmann (2015), using the same model data, also identified a coherent atmospheric teleconnection for 2013-14 that includes a warm West-cold East surface temperature dipole.

Our analysis focuses on the 1979-2014 period, which may not very well contain all the “Faces of ENSO”, among other modes of SST variations to which forced teleconnections may be sensitive. In addition, the time-dependent volcanic aerosols forcing is not included in the present AMIP simulations. In a next step we plan to carry out a parallel analysis of large historical simulations spanning the post-1900 period using a large ensemble AMIP and large ensemble CMIP data set, in which identical AGCM

components forced with the changes in volcanic aerosols and anthropogenic greenhouse gases are involved. This may provide a clearer separation of the sensitivity of forced atmospheric teleconnections arising from external forcing alone versus from the additional effect of the particular trajectory in observed SST conditions.

## APPENDIX A

### **Comparison of leading modes of variability of 500hPa heights in reanalysis and GFS model simulations**

The EOF patterns between the reanalysis data and GFS model simulations are compared to examine the model fidelity in simulating the leading modes of variability of Dec-Feb mean 500hPa heights. Figure A1 (left panels) shows the regression patterns corresponding to the first 3 EOFs of reanalysis data, which explain a combined 54.8% of the wintertime height variability poleward of 20°N. The same EOF procedure is applied to the climate simulations. In this application, we concatenate the individual members of the AMIP simulations, which for the GFS data consist of 1750 winter seasons. Figure A1 (middle panels) shows the regression patterns corresponding to the first 3 EOFs of GFS simulations, which explain a combined 46.8% of the model's wintertime height variability poleward of 20°N. The model is seen to replicate the leading observed pattern of 500 hPa height variability which consists of a prominent wave train over the Pacific-North American region. The observed second EOF pattern is likewise part of the model's leading modes of variability, though ranked third in its EOF decomposition and explaining less overall height variance. We note that there exists considerable sampling

variability in the EOF rankings and detailed structures based on separate samples of only 35 winters (not shown). We have quantified the range of pattern similarity between model simulations and observations for the first 3 EOFs. The EOF1 pattern congruence between individual members of the AMIP simulations and observations based on 35 winters ranges from 0.59 to 0.95. However, the range of EOF2 and EOF3 pattern congruence is more scattered, with values from 0.00 to 0.89 for the former and from 0.02 to 0.88 for the latter. This large uncertainty is expected because of the considerable sampling variability in the EOF rankings in the model simulations, in addition to the possible model biases.

The leading patterns of the GFS 500-hPa height variability can be largely reproduced in a climate simulation having no interannual variability in boundary conditions or external radiative forcing. A 100-yr long climatological run of GFS has been performed using repeating seasonal cycle SSTs and carbon dioxide concentrations corresponding to the mean of 1979-2014. Figure A1 (right panels) shows the regression patterns corresponding to the first 3 EOFs of this climatological run, which explain a combined 43.8% of the wintertime height variability poleward of 20°N. The spatial structures are very similar to the AMIP version of the model, and it is evident that internal atmospheric variability is a major source of NH wintertime height variability.

## APPENDIX B

### **Comparison of forced modes of variability between GFS and ECHAM4.5 models**

The robustness of the boundary forced atmospheric circulation sensitivities shown in Fig. 2 is evaluated by repeating the EOF analysis using different model data. Important in such intercomparison is the use of large-sized ensemble simulations so as not to confound forced patterns with internal atmospheric variability that may dominate an EOF analysis based on small-sized ensembles. We have therefore used the data from an 85-member ensemble of similarly designed AMIP experiments derived from the ECHAM4.5 model (Roeckner et al. 1996; data provided by IRI, see <http://iridl.ldeo.columbia.edu/SOURCES/.IRI/.FD/.ECHAM4p5/.History/.ensemble85/>). Differences in parameterizations and spatial resolutions (e.g., ECHAM4.5 is run at T42 scale) permit a meaningful evaluation of whether these large spatial modes of atmospheric sensitivity derived from GFS data are robust to model formulation. Figure B1 compares the height structures corresponding to the first two EOFs of wintertime 500 hPa heights for a common simulation period of 1979-2003. The spatial patterns of the models' corresponding EOFs are very similar (spatial correlation exceeds 0.9 over the map domain), as are the temporal variations in their PC time series (temporal correlation of forced solutions exceeds 0.9 during 1979-2003). This intercomparison reveals that the atmospheric sensitivities do not depend on the selection of a particular model. They are more determined by the nature of the boundary forcing used for each atmospheric model instead.

## APPENDIX C

### **The leading mode of variability of 500hPa heights in individual coupled runs**

781

782 The leading EOF (EOF1) mode of variability of winter (DJF) season 500-hPa heights in  
783 50 individual coupled runs (30 CESM1 runs and 20 CCSM4 runs) is examined to explore  
784 the role of external radiative forcing on the trend in the leading ENSO teleconnection  
785 pattern. Figure C1 (bottom left) provides a validation of the realism of the coupled  
786 models, in so far as this "recurrent" EOF1 pattern of each member is spatially very  
787 similar to the observed EOF1 height pattern shown in Figure A1 (The EOF1 pattern  
788 congruence between individual coupled runs and observations ranges from 0.66 to 0.92  
789 and the dominant congruence values are within 0.8~0.9). The ensemble mean of EOF1  
790 pattern averaged over 50 individual coupled runs has a strong spatial congruence ( $r=0.88$ )  
791 with observations (Figure C1, top left), and the time series of this mode of coupled  
792 variability, on average, has no significant trend during 1979-2014 (Figure C1, top right).  
793 The results indicate that external radiative forcing has no significant effect on the trend in  
794 the leading ENSO teleconnection pattern. We also note that the time series of EOF1 from  
795 the individual coupled model samples can have a strong positive (negative) trend, ranging  
796 to as much as 1.51 (and -1.36) standardized units, showing a large range of internal  
797 variability effects on this multi-decadal time scale (Figure C1, bottom right). The value of  
798 forced trend in the PC time series of EOF1 from AMIP simulations resides within the  
799 distribution of individual coupled model samples. This result supports the argument that  
800 the trend in EOF1 pattern of AMIP (GFSv2) 500-hPa height (see Figure 1 and Figure 11  
801 top left) is not appreciably due to climate change forcing. Instead, the trend in this AMIP  
802 EOF1 is a symptom of internal variability.

803

804   **Acknowledgments**

805   This work was supported by grants from NOAA's Climate Program Office. We  
806   acknowledge NCAR's CESM1(CAM5) Large Ensemble Community Project for carrying  
807   out the large CESM1 ensemble. We wish to thank Xiaowei Quan for carrying out the  
808   large CCSM4 ensemble, and Jon Eischeid for his technical support. We also thank three  
809   anonymous reviewers for their constructive comments that helped to improve the paper.

810

811

812

813

814

815



**References:**

- Alexander, M. A., D. J. Vimont, P. Chang, and J. D. Scott, 2010: The impact of extratropical atmospheric variability on ENSO: Testing the seasonal footprinting mechanism using coupled model experiments. *J. Climate*, **23**, 2885–2901.
- An, S-I., and F-F. Jin, 2004: Nonlinearity and asymmetry of ENSO. *J. Climate*, **17**, 2399–2412.
- Ashok, K., S. K. Behera, S. A. Rao, H. Weng, and T. Yamagata, 2007: El Niño Modoki and its possible teleconnection, *J. Geophys. Res.*, **112**, C11007, doi:[10.1029/2006JC003798](https://doi.org/10.1029/2006JC003798).
- Barnston, A. G., and R. E. Livezey, 1987: Classification, seasonality, and persistence of low-frequency atmospheric circulation patterns. *Mon. Wea. Rev.*, **115**, 1083–1126.
- Burgers, G., and D. B. Stephenson, 1999: The “normality” of El Niño. *Geophys. Res. Lett.*, **26**, 1027–1030.
- Capotondi, A., and Co-authors, 2015: Understanding ENSO Diversity. *Bull. Amer. Meteor. Soc.*, **96**, 921–938. doi: <http://dx.doi.org/10.1175/BAMS-D-13-00117.1>
- Collins, M., and Coauthors, 2010: The impact of global warming on the tropical Pacific Ocean and El Niño. *Nat. Geosci.*, **3**, 391–397.
- Dee, D. P., and 35 co-authors, 2011: The ERA-Interim reanalysis: Configuration and performance of the data assimilation system. *Quart. J. R. Meteorol. Soc.*, **137**, 553–597. DOI: 10.1002/qj.828.
- Dommenget, D., T. Bayr, and C. Frauen, 2013: Analysis of the non-linearity in the pattern and time evolution of El Niño Southern Oscillation. *Climate Dyn.*, **40**, 2825–2847.

839 Geisler, J. E., M. L. Blackmon, G. T. Bates, and S. Munoz, 1985: Sensitivity of January  
840 climate response to the magnitude and position of equatorial Pacific sea surface  
841 temperature anomalies. *J. Atmos. Sci.*, **42**, 1037–1049.

842 Gent, P., and Coauthors, 2011: The Community Climate System Model version 4. *J.*  
843 *Climate*, **24**, 4973–4991.

844 Guilyardi, E., 2006: El Niño-mean state-seasonal cycle interactions in a multi-model  
845 ensemble. *Climate Dyn.*, 26, 329–348.

846 Hartmann, D. L., 2015: Pacific sea surface temperature and the winter of 2014. *Geophys.*  
847 *Res. Lett.*, **42**, doi:10.1002/2015GL063083.

848 Hoerling, M. P., and A. Kumar, 2000: Understanding and predicting extratropical  
849 teleconnections related to ENSO. *El Niño and the Southern Oscillation: Multi-Scale*  
850 *Variability, and Global and Regional Impacts*, H. Diaz and V. Markgraf, Eds.,  
851 Cambridge University Press, 57–88.

852 Hoerling, M. P., and A. Kumar, 2002: Atmospheric response patterns associated with  
853 tropical forcing. *J. Climate*, **15**, 2184–2203.

854 Hoerling, M. P., A. Kumar, and M. Zhong, 1997: El Niño, La Niña, and the nonlinearity  
855 of their teleconnections. *J. Climate*, **10**, 1769–1786.

856 Hoerling, M. P., A. Kumar, and T.-Y. Xu, 2001: Robustness of the nonlinear  
857 atmospheric response to opposite phases of ENSO. *J. Climate*, **14**, 1277–1293.

858 Hoerling, M. P., J. Eischeid, and J. Perlwitz, 2010: Regional precipitation trends:  
859 Distinguishing natural variability from anthropogenic forcing. *J. Climate*, **23**, 2131–  
860 2145.

861 Horel J. D. and J. M. Wallace, 1981: Planetary-Scale Atmospheric Phenomena  
862 Associated with the Southern Oscillation. *Mon. Wea. Rev.*, **109**, 813–829.

863 Hurrell, J., J. Hack, D. Shea, J. Caron, and J. Rosinski, 2008: A new sea surface  
864 temperature and sea ice boundary data set for the Community Atmosphere Model. *J.*  
865 *Climate*, **21**, 5145–5153.

866 IPCC, 2013: Climate Change 2013: The Physical Science Basis. Contribution of Working Group  
867 I to the Fifth Assessment Report of the Intergovernmental Panel on Climate Change [Stocker,  
868 T.F., D. Qin, G.-K. Plattner, M. Tignor, S.K. Allen, J. Boschung, A. Nauels, Y. Xia, V. Bex  
869 and P.M. Midgley (eds.)]. Cambridge University Press, Cambridge, United Kingdom and New  
870 York, NY, USA, 1535 pp, doi:10.1017/CBO9781107415324.

871 Johnson, N. C., 2013: How Many ENSO Flavors Can We Distinguish? *J. Climate*, **26**,  
872 4816–4827. doi: <http://dx.doi.org/10.1175/JCLI-D-12-00649.1>

873 Kalnay, E., et al., 1996: The NCEP/NCAR 40-year reanalysis project, *Bull. Am.*  
874 *Meteorol. Soc.*, **77**, 437–471.

875 Kao, H.-Y., and J.-Y. Yu, 2009: Contrasting eastern-Pacific and central-Pacific types of  
876 ENSO, *J. Climate*, **22**, 615–632, doi:[10.1175/2008JCLI2309.1](http://dx.doi.org/10.1175/2008JCLI2309.1).

877 Kay, J. E., Deser, C., Phillips, A., Mai, A., Hannay, C., Strand, G., Arblaster, J., Bates,  
878 S., Danabasoglu, G., Edwards, J., Holland, M. Kushner, P., Lamarque, J.-F.,  
879 Lawrence, D., Lindsay, K., Middleton, A., Munoz, E., Neale, R., Oleson, K., Polvani,  
880 L., and M. Vertenstein, 2015: The Community Earth System Model (CESM) Large  
881 Ensemble Project: A Community Resource for Studying Climate Change in the  
882 Presence of Internal Climate Variability, *Bulletin of the American Meteorological*  
883 *Society*, doi:10.1175/BAMS-D-13-00255.1 (in press)

884 Kim, S. T., W. Cai, F.-F. Jin, A. Santoso, L. Wu, E. Guilyardi, and S.-I. An, 2014:  
885 Response of El Niño sea surface temperature variability to greenhouse warming. *Nat.*  
886 *Climate Change*, **4**, 786–790, doi:10.1038/nclimate2326.

887 Kug, J.-S., F.-F. Jin, and S.-I. An, 2009: Two types of El Niño events: Cold Tongue El  
888 Niño and Warm Pool El Niño, *J. Climate*, **22**, 1499–1515,  
889 doi:[10.1175/2008JCLI2624.1](https://doi.org/10.1175/2008JCLI2624.1).

890 Kumar, A., Q. Zhang, P. Peng, and B. Jha, 2005: SST-Forced Atmospheric Variability in  
891 an Atmospheric General Circulation Model. *J. Climate*, **18**, 3953–3967.

892 Larkin, N. K., and D. E. Harrison, 2005: Global seasonal temperature and precipitation  
893 anomalies during El Niño autumn and winter, *Geophys. Res. Lett.*, **32**, L16705,  
894 doi:[10.1029/2005GL022860](https://doi.org/10.1029/2005GL022860).

895 Mantua, N. J., S. R. Hare, Y. Zhang, J. Wallace, and R. C. Francis, 1997: A Pacific  
896 interdecadal climate oscillation with impacts on salmon production. *Bull. Amer.*  
897 *Meteor. Soc.*, **78**, 1069–1079.

898 Meehl, G. A., and Coauthors, 2013: Climate change projections in CESM1 (CAM5)  
899 compared to CCSM4. *J. Climate*, **26**, 6287–6308, doi:10.1175/JCLI-D-12-00572.1.

900 Mo, K. C. and R. E. Livezey, 1986: Tropical-Extratropical Geopotential Height  
901 Teleconnections during the Northern Hemisphere Winter. *Mon. Wea. Rev.*, **114**, 2488–  
902 2515.

903 Neale, R. B., and Coauthors, 2010: Description of the NCAR Community Atmosphere  
904 Model (CAM 4.0). NCAR Tech. Note NCAR/TN-485+STR, 212 pp.

905 Neale, R. B., and Coauthors, 2012: Description of the NCAR Community Atmosphere  
 906 Model (CAM 5.0). NCAR Tech. Note NCAR/TN-486+STR, 274 pp.

907 Palmer, T. N., and D. A. Mansfield, 1986a: A study of wintertime circulation anomalies  
 908 during past El Niño events using a high resolution general circulation model: I:  
 909 Influence of model climatology. *Quart. J. Roy. Meteor. Soc.*, **112**, 613–638.

910 Palmer, T. N., and D. A. Mansfield, 1986b: A study of wintertime circulation anomalies  
 911 during past El Niño events using a high resolution general circulation model: II:  
 912 Variability of the seasonal mean response. *Quart. J. Roy. Meteor. Soc.*, **112**, 639–660.

913 Penland, C., and P. D. Sardeshmukh, 1995: The optimal growth of tropical sea surface  
 914 temperature anomalies. *J. Climate*, **8**, 1999–2024.

915 Perlwitz, J., M. P. Hoerling, and R. Dole, 2015: Arctic Tropospheric Warming: Causes  
 916 and Linkages to Lower Latitudes. *J. Climate*, **28**, 2154–2167. doi:  
 917 <http://dx.doi.org/10.1175/JCLI-D-14-00095.1>

918 Roeckner, E., and Coauthors, 1996: The atmospheric general circulation model  
 919 ECHAM4: Model description and simulation of present-day climate. Max-Planck-  
 920 Institut für Meteorologie Rep. 218, Hamburg, Germany, 90 pp.

921 Saha, S., and Coauthors, 2014: The NCEP Climate Forecast System version 2. *J. Climate*,  
 922 **27**, 2185–2208, doi:10.1175/JCLI-D-12-00823.1.

923 Seager, R., M. Hoerling, S. Schubert, H. Wang, B. Lyon, A. Kumar, J. Nakamura, and N.  
 924 Henderson; 2014: Causes and predictability of the 2011-14 California drought. Report  
 925 of the NOAA Drought Task Force, doi:10.7289/V58K771F, 40 pp., [Available at  
 926 [http://docs.lib.noaa.gov/noaa\\_documents/OAR/CPO/MAPP/california\\_drought\\_2011-2014.pdf](http://docs.lib.noaa.gov/noaa_documents/OAR/CPO/MAPP/california_drought_2011-2014.pdf)]

927 Stevenson, S. L., 2012: Significant changes to ENSO strength and impacts in the twenty-  
 928 first century: Results from CMIP5. *Geophys. Res. Lett.*, **39**, L17703,  
 929 doi:10.1029/2012GL052759.

930 Takahashi, K., A. Montecinos, K. Goubanova, and B. Dewitte, 2011: ENSO regimes:  
 931 Reinterpreting the canonical and Modoki El Niño. *Geophys. Res. Lett.*, **38**, L10704,  
 932 doi:10.1029/2011GL047364.

933 Ting, M., and P. D. Sardeshmukh, 1993: Factors determining the extratropical response  
 934 to equatorial diabatic heating anomalies. *J. Atmos. Sci.*, **50**, 907-918.

935 Trenberth, K. E., and D. P. Stepaniak, 2001: Indices of El Niño Evolution. *J. Climate*, **14**,  
 936 1697–1701.

937 Trenberth, K. E., 1993: The different flavors of El Niño. *Proc. 18<sup>th</sup> Annual Climate*  
 938 *Diagnostics Workshop*, Boulder, CO., National Oceanic and Atmospheric  
 939 Administration, 50-53.

940 Trenberth, K. E., G. W. Branstator, D. Karoly, A. Kumar, N.-C. Lau, and C. Ropelewski,  
 941 1998: Progress during TOGA in understanding and modeling global teleconnections  
 942 associated with tropical sea surface temperatures. *J. Geophys. Res.*, **103**, 14 291–14  
 943 324.

944 Vimont, D. J., D. S. Battisti, and A. C. Hirst, 2001: Footprinting: A seasonal link between  
 945 the tropics and mid-latitudes. *Geophys. Res. Lett.*, **28**, 3923–3926.

946 Vimont, D. J., D. S. Battisti, and A. C. Hirst, 2003a: The seasonal footprinting  
 947 mechanism in the CSIRO general circulation models. *J. Climate*, **16**, 2653–2667.

948 Vimont, D. J., J. M. Wallace, and D. S. Battisti, 2003b: The seasonal footprinting  
 949 mechanism in the Pacific: Implications for ENSO. *J. Climate*, **16**, 2668–2675.

950 Wang, S.-Y., L. Hipps, R. R. Gillies, and J.-H. Yoon, 2014: Probable causes of the  
 951 abnormal ridge accompanying the 2013–2014 California drought: ENSO precursor  
 952 and anthropogenic warming footprint, *Geophys. Res. Lett.*, **41**, 3220–3226,  
 953 doi:10.1002/2014GL059748.

954 Wittenberg, A. T., 2009: Are historical records sufficient to constrain ENSO simulations?  
 955 *Geophys. Res. Lett.*, 36, L12702, doi:[10.1029/2009GL038710](https://doi.org/10.1029/2009GL038710).

956 Yeh, S.-W., J.-S. Kug, B. Dewitte, M.-H. Kwon, B. P. Kirtman, and F.-F. Jin, 2009: El  
 957 Niño in a changing climate, *Nature*, 461, 511–514, doi:[10.1038/nature08316](https://doi.org/10.1038/nature08316).

958 Yeh, S.-W., B. P. Kirtman, J.-S. Kug, W. Park, and M. Latif, 2011: Natural variability of  
 959 the central Pacific El Niño event on multi-centennial timescales, *Geophys. Res. Lett.*, 38,  
 960 L02704, doi:[10.1029/2010GL045886](https://doi.org/10.1029/2010GL045886).

961 Yu, J.-Y., and H.-Y. Kao, 2007: Decadal changes of ENSO persistence barrier in SST  
 962 and ocean heat content indices: 1958–2001, *J. Geophys. Res.*, 112, D13106,  
 963 doi:[10.1029/2006JD007654](https://doi.org/10.1029/2006JD007654).

964 Yu, J.-Y., Y. Zou, S. T. Kim, and T. Lee, 2012: The changing impact of El Niño on US  
 965 winter temperatures, *Geophys. Res. Lett.*, 39, L15702, doi:[10.1029/2012GL052483](https://doi.org/10.1029/2012GL052483).

966 Zhang, T., D.-Z. Sun, R. Neale, and P. J. Rasch, 2009: An evaluation of ENSO  
 967 asymmetry in the Community Climate System Models: A view from the subsurface. *J.*  
 968 *Climate*, **22**, 5933–5961.

969 Zhang, T., J. Perlwitz, and M. P. Hoerling, 2014: What is responsible for the strong  
 970 observed asymmetry in teleconnections between El Niño and La Niña? *Geophys. Res.*  
 971 *Lett.*, **41**, 1019–1025, doi:10.1002/2013GL058964.

972 Zhang, T., and D.-Z. Sun, 2014: ENSO Asymmetry in CMIP5 Models. *J. Climate*, **27**,  
973 4070-4093, doi:10.1175/JCLI-D-13-00454.1.

974 Zhang, Y., J. M. Wallace, and D. S. Battisti, 1997: ENSO-like interdecadal variability:  
975 1900–1993. *J. Climate*, **10**, 1004–1020.

976

977



## Figure Captions

Figure 1. (left) The spatial pattern and (right) standardized PC time series of the leading two EOFs of GFSv2 simulated 50-member ensemble mean winter (DJF) season 500-hPa heights. The analysis is computed over the 20°N-90°N domain for 1979/80 through 2013/14. The EOF patterns are shown as the regressions of the heights onto the standardized PC time series, and drawn at the interval of 5 meter for a 1 standardized departure of PC index.

Figure 2. The scatter relationship between observed tropical Pacific SST indices and the PC indices from GFSv2 simulations shown in Figure 1. The top panel shows the relationship between N3.4 (SST anomalies in the Niño 3.4 region) standardized index and PC1 index, and the bottom panel shows the relationship between TNI (Trans-Niño Index) standardized index and PC2 index. The observational SST data used in the calculations are from Hurrell et al. (2008).

Figure 3. (left) The observed regression patterns of winter (DJF) season 500-hPa heights onto (top) the Niño3.4 SST anomalies and onto (bottom) TNI index over the 20°N-90°N domain for the period of 1979-2014. (right) Corresponding regression patterns of GFSv2 simulated 50-member ensemble mean winter (DJF) season 500-hPa heights. The observational estimates are based on NCEP/NCAR height fields and Hurrell et al. (2008) SST data. The contour interval is 5 meter per degree Celsius for top panels and 5 meter per standard unit for bottom panels.

1001 Figure 4. The scatter relationship between PC1 index and PC2 index from GFSv2  
1002 simulations shown in Figure 1.  
1003

1004 Figure 5. (left) The composite DJF anomalies of (first row) Northern Hemisphere 500-  
1005 hPa height, (second row) tropical SST, (third row) North American surface temperature,  
1006 (fourth row) tropical precipitation, and (fifth row) North American precipitation for 7  
1007 strongest cases with positive PC1 values from GFSv2 simulations shown in Figure 4.  
1008 (right) Corresponding anomalies for 7 strongest cases with negative PC1 values shown in  
1009 Figure 4. The contour interval of height fields in the first row is 10 meter.  
1010

1011 Figure 6. The sum between composite DJF anomalies of 7 strongest cases with positive  
1012 PC1 values (left panels of Figure 5) and composite DJF anomalies of 7 strongest cases  
1013 with negative PC1 values (right panels of Figure 5). The contour interval of height fields  
1014 in the first row is 10 meter.  
1015

1016 Figure 7. (left) The composite DJF anomalies of (first row) Northern Hemisphere 500-  
1017 hPa height, (second row) tropical SST, (third row) North American surface temperature,  
1018 (fourth row) tropical precipitation, and (fifth row) North American precipitation for 7  
1019 strongest cases with positive PC2 values from GFSv2 simulations shown in Figure 4.  
1020 (right) Corresponding anomalies for 7 strongest cases with negative PC2 values shown in  
1021 Figure 4. The contour interval of height fields in the first row is 10 meter.  
1022

Figure 8. Top panels show (left) the spatial pattern and (right) standardized PC time series of EOF3 of GFSv2 simulated 50-member ensemble mean winter (DJF) season 500-hPa heights. The bottom panels show (left) the spatial pattern and (right) standardized PC time series of the leading EOF of 50-member ensemble mean winter (DJF) season 500-hPa heights in coupled model runs which include 20 runs from CCSM4 and 30 runs from CESM1. The analysis is computed over the 20°N-90°N domain for 1979/80 through 2013/14. The EOF patterns are shown as the regressions of the heights onto the standardized PC time series, and drawn at the interval of 1 meter for a 1 standardized departure of PC index.

Figure 9. (Top) The ratio of forced component to the total variance of winter (DJF) seasonally averaged 500-hPa height for 1979/80 through 2013/14 in GFSv2 AMIP runs. The results are shown for (left) the NH polar cap to 20°N, and for (right) the global domain. (Bottom) corresponding results from coupled model runs which are the combinations of the runs from CCSM4 and CESM1. The contour interval is 0.05 for left panels and 0.2 for right panels. Forced variability is computed from the variance of ensemble means. Total variability is computed from the concatenated time series of the individual members. For two coupled models, the total variability is computed for each separately, and then averaged.

Figure 10. The ratio of the leading three EOFs of forced component to the total variance of winter (DJF) seasonally averaged 500-hPa height for 1979/80 through 2013/14 in GFSv2 AMIP runs. The height anomalies projecting on different modes can be computed

as the scalar product of different EOF patterns and the associated PC time series. The contour interval is 0.05.

Figure 11. The trend pattern of EOF1, the sum of EOF1 and EOF3, and the trend pattern of ensemble mean of winter (DJF) season 500-hPa heights from GFSv2 AMIP runs over the 20°N-90°N domain for 1979/80 through 2013/14. The observed trend pattern is shown in lower right. The trend patterns of EOF1 and EOF3 are obtained by the product between the EOF pattern and the total trend of the corresponding PC time series (the total trend is -1.09 standardized unit for PC1 and 2.0 standardized unit for PC3) shown in the top panels of Figure 1 and Figure 8, respectively. The contour interval is 5 meter.

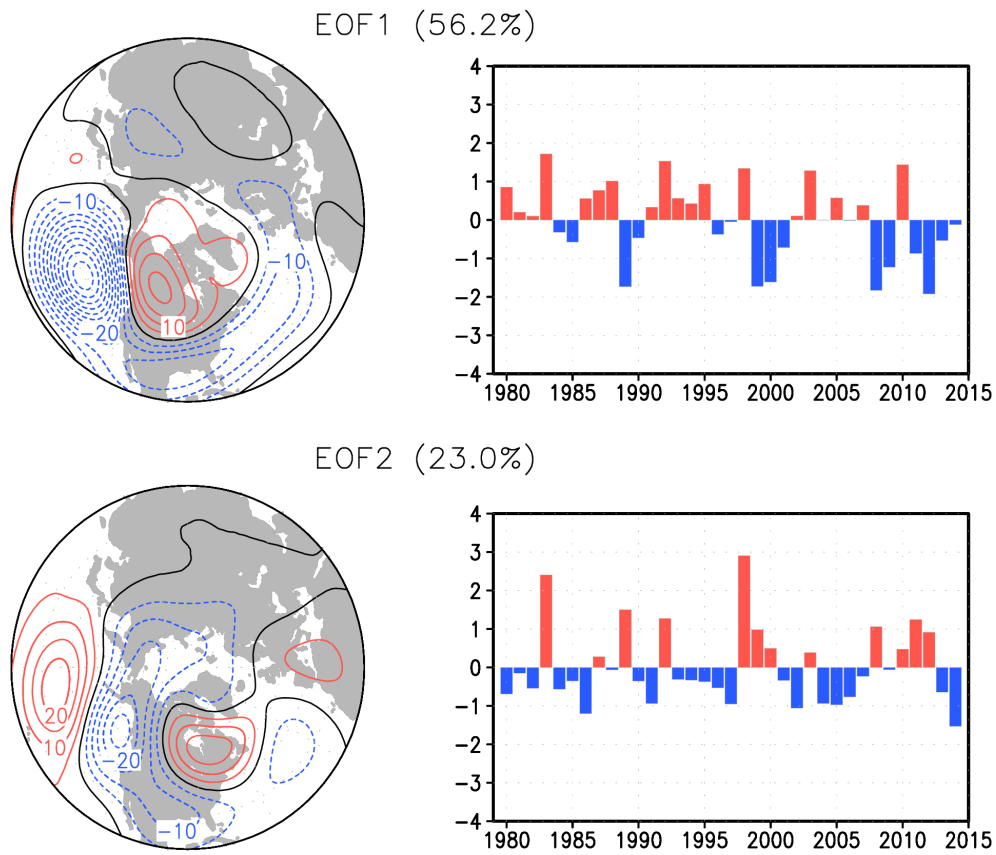
Figure A1. The spatial pattern of the leading three EOFs of winter (DJF) season 500-hPa heights from (left) observations, (middle) the concatenation of all 50 AMIP runs of GFSv2 and (right) a 100-yr-long GFSv2 climatological run in which the model is driven by observed SST climatology. Note that the model data used here are not ensemble means. The observational estimate is based on NCEP reanalysis for 1979/80 through 2013/14. The analysis is computed over the 20°N-90°N domain. The EOF patterns are shown as the regressions of the heights onto the standardized PC time series, and drawn at the interval of 5 meter for a 1 standardized departure of PC index.

Figure B1. (left) The spatial pattern and (right) standardized PC time series of the leading two EOFs of winter (DJF) season 500-hPa ensemble mean heights from GFSv2 AMIP runs and ECHAM4.5 AMIP runs for the common period of 1979-2003. The analysis is

computed over the 20°N-90°N domain based on 50-member ensemble mean from GFSv2 model and 85-member ensemble mean from ECHAM4.5 model. The EOF patterns are shown as the regressions of the heights onto the standardized PC time series, and drawn at the interval of 5 meter for a 1 standardized departure of PC index.

Figure C1. Ensemble mean of (top left) the spatial pattern and (top right) standardized PC time series of the leading EOF of winter (DJF) season 500-hPa heights averaged over 50 individual coupled runs which include 20 runs from CCSM4 and 30 runs from CESM1. (bottom left) Probability distribution function (PDF) for the EOF1 pattern congruence between individual coupled runs (indicated by short red lines) and NCEP reanalysis shown in Figure A1. (bottom right) PDF for 1979-2014 trend of standardized PC time series of the leading EOF (PC1) from the individual coupled model samples (indicated by short red lines), and the value of ensemble mean forced trend of PC1 in the AMIP simulations is also shown (indicated by long black line). Abscissa is of the total change during 1979-2014. The EOF analysis is computed over the 20°N-90°N domain for 1979/80 through 2013/14 and pattern congruence analysis is computed over the same domain. The EOF patterns are shown as the regressions of the heights onto the standardized PC time series, and drawn at the interval of 5 meter for a 1 standardized departure of PC index. The PDF is a nonparametric curve constructed using the R software program, which utilizes a kernel density estimation and a Gaussian smoother.

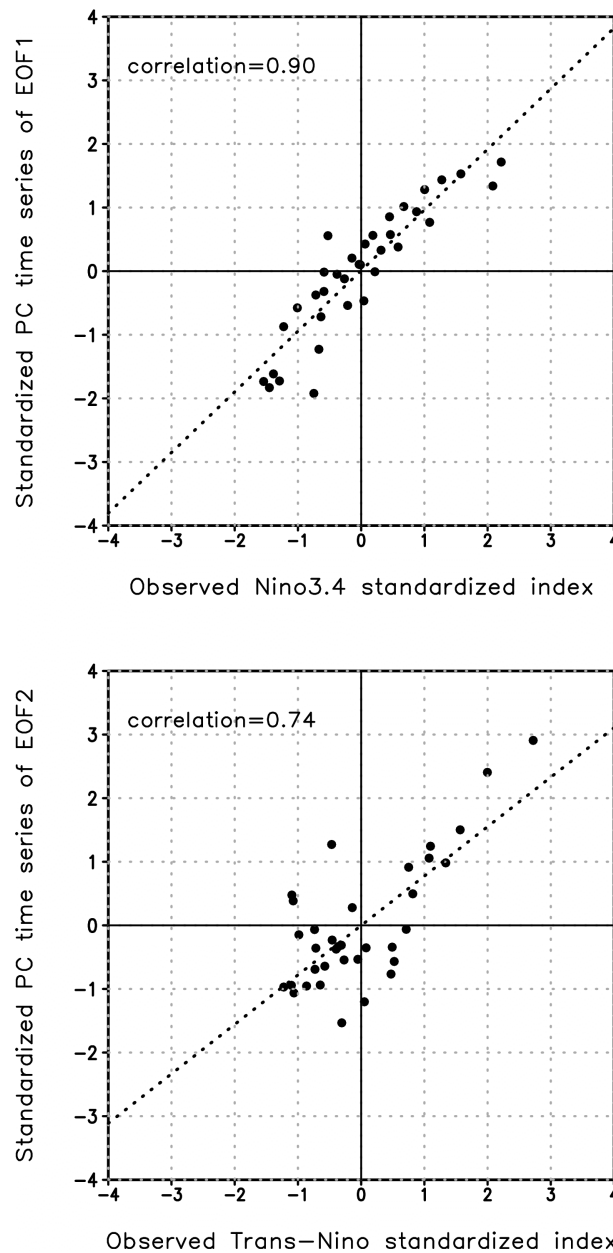
1090



1091  
1092  
1093  
1094  
1095  
1096  
1097  
1098  
1099  
1100  
1101  
1102  
1103  
1104  
1105  
1106  
1107  
1108  
1109  
1110  
1111  
1112  
1113  
1114

Figure 1. (left) The spatial pattern and (right) standardized PC time series of the leading two EOFs of GFSv2 simulated 50-member ensemble mean winter (DJF) season 500-hPa heights. The analysis is computed over the 20°N-90°N domain for 1979/80 through 2013/14. The EOF patterns are shown as the regressions of the heights onto the standardized PC time series, and drawn at the interval of 5 meter for a 1 standardized departure of PC index.

1115



1116  
1117  
1118  
1119  
1120  
1121  
1122  
1123  
1124  
1125  
1126  
1127  
1128

Figure 2. The scatter relationship between observed tropical Pacific SST indices and the PC indices from GFSv2 simulations shown in Figure 1. The top panel shows the relationship between N3.4 (SST anomalies in the Niño 3.4 region) standardized index and PC1 index, and the bottom panel shows the relationship between TNI (Trans-Niño Index) standardized index and PC2 index. The observational SST data used in the calculations are from Hurrell et al. (2008).

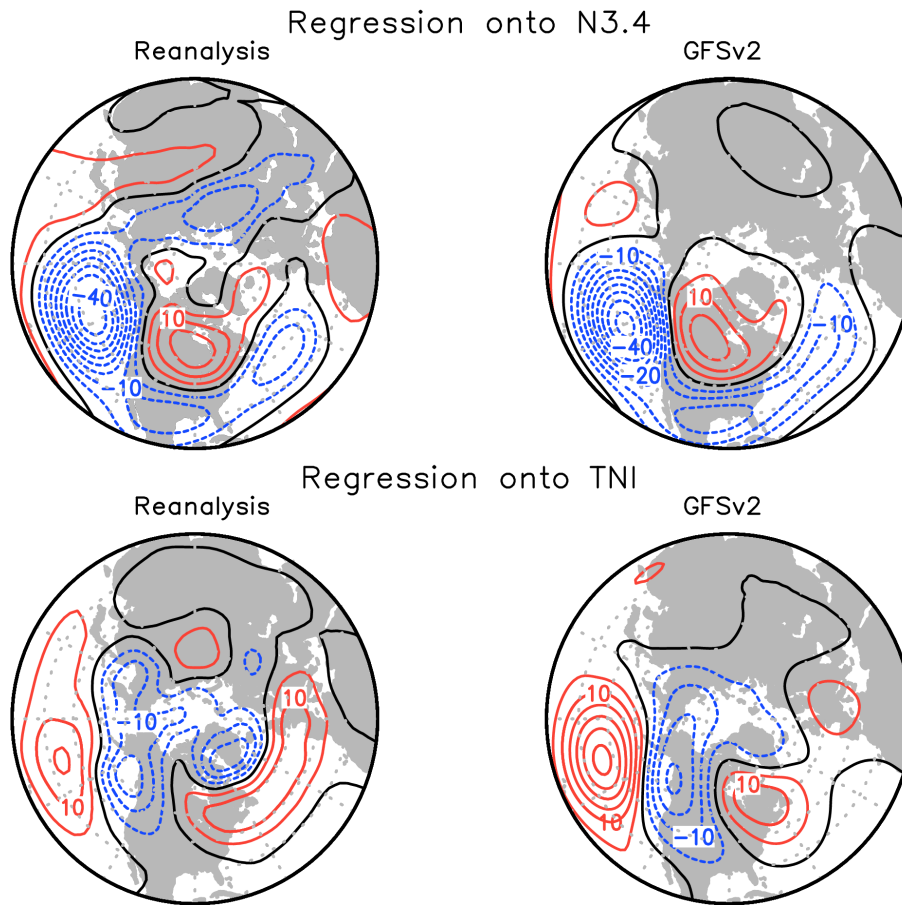
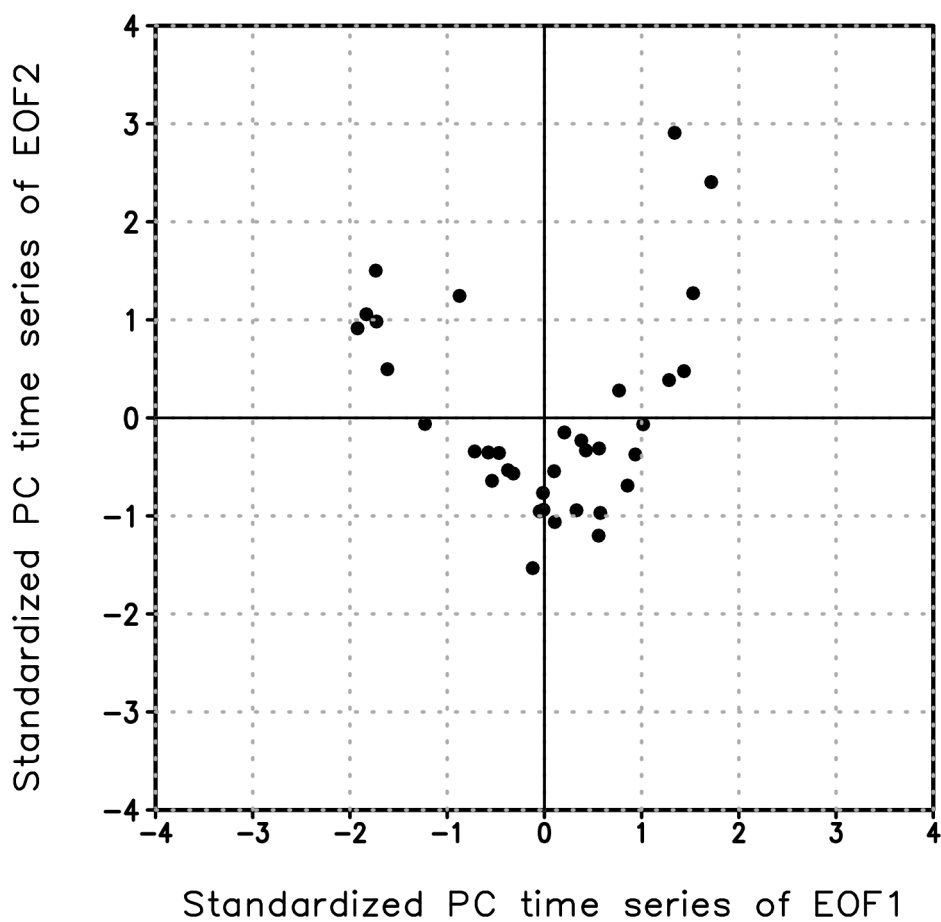


Figure 3. (left) The observed regression patterns of winter (DJF) season 500-hPa heights onto (top) the Niño3.4 SST anomalies and onto (bottom) TNI index over the 20°N-90°N domain for the period of 1979-2014. (right) Corresponding regression patterns of GFSv2 simulated 50-member ensemble mean winter (DJF) season 500-hPa heights. The observational estimates are based on NCEP/NCAR height fields and Hurrell et al. (2008) SST data. The contour interval is 5 meter per degree Celsius for top panels and 5 meter per standard unit for bottom panels.



1152



1153  
1154  
1155  
1156  
1157  
1158  
1159  
1160  
1161  
1162  
1163  
1164  
1165  
1166  
1167  
1168  
1169  
1170  
1171  
1172  
1173  
1174

Figure 4. The scatter relationship between PC1 index and PC2 index from GFSv2 simulations shown in Figure 1.

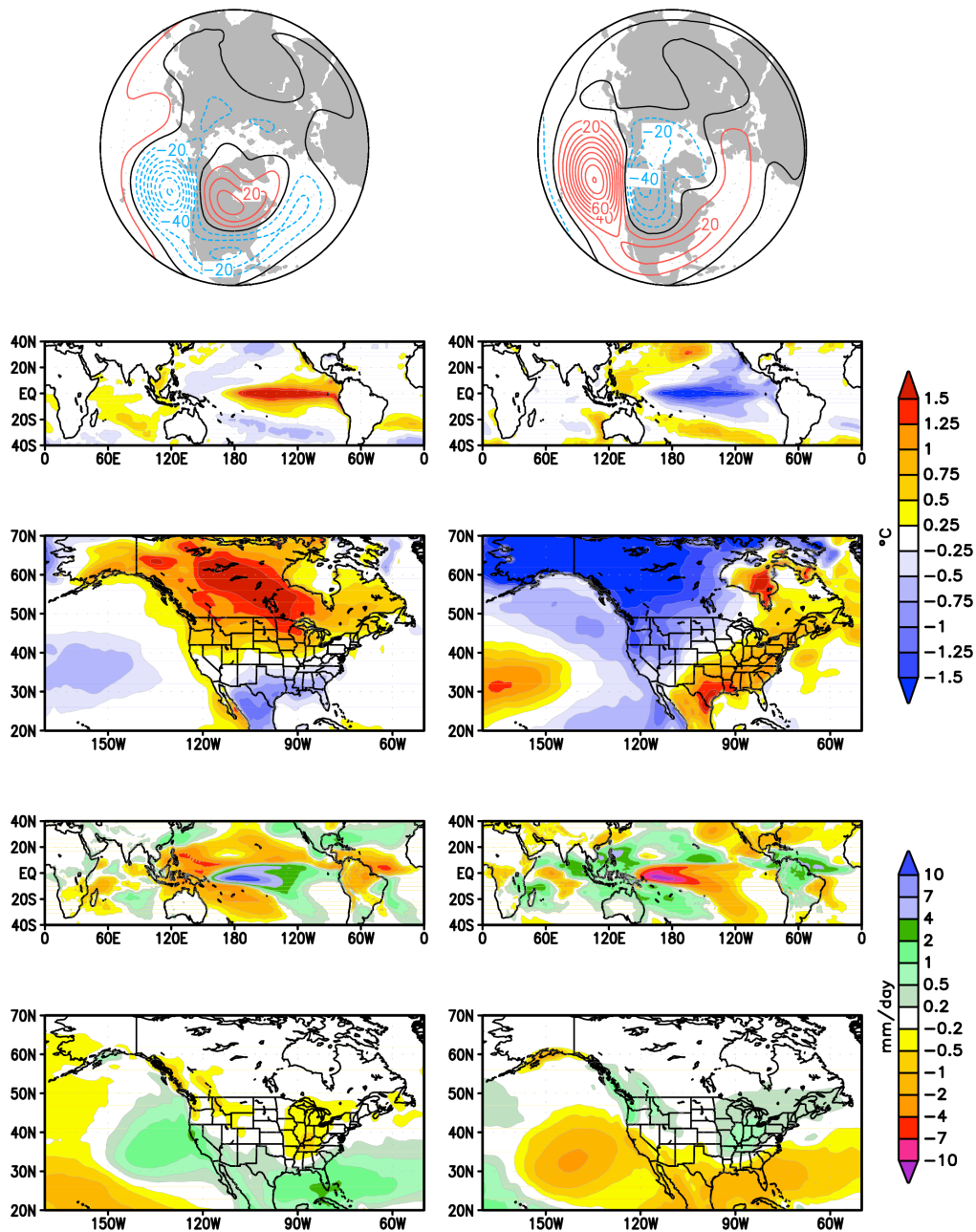


Figure 5. (left) The composite DJF anomalies of (first row) Northern Hemisphere 500-hPa height, (second row) tropical SST, (third row) North American surface temperature, (fourth row) tropical precipitation, and (fifth row) North American precipitation for 7 strongest cases with positive PC1 values from GFSv2 simulations shown in Figure 4. (right) Corresponding anomalies for 7 strongest cases with negative PC1 values shown in Figure 4. The contour interval of height fields in the first row is 10 meter.

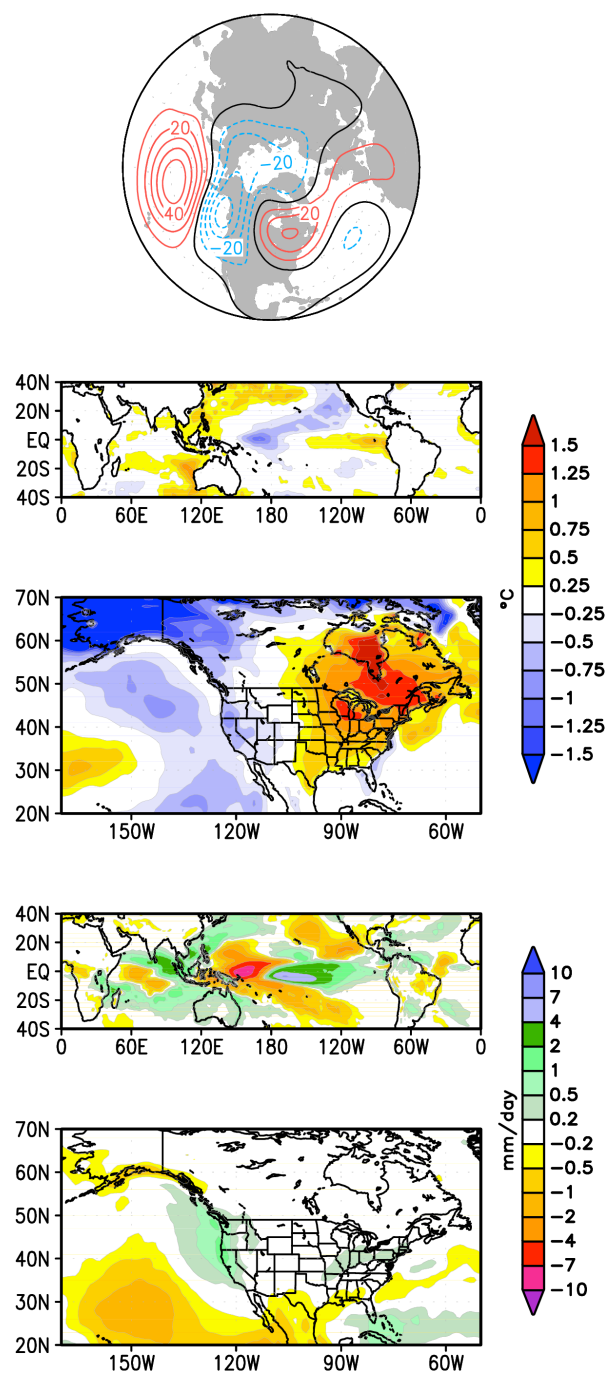


Figure 6. The sum between composite DJF anomalies of 7 strongest cases with positive PC1 values (left panels of Figure 5) and composite DJF anomalies of 7 strongest cases with negative PC1 values (right panels of Figure 5). The contour interval of height fields in the first row is 10 meter.

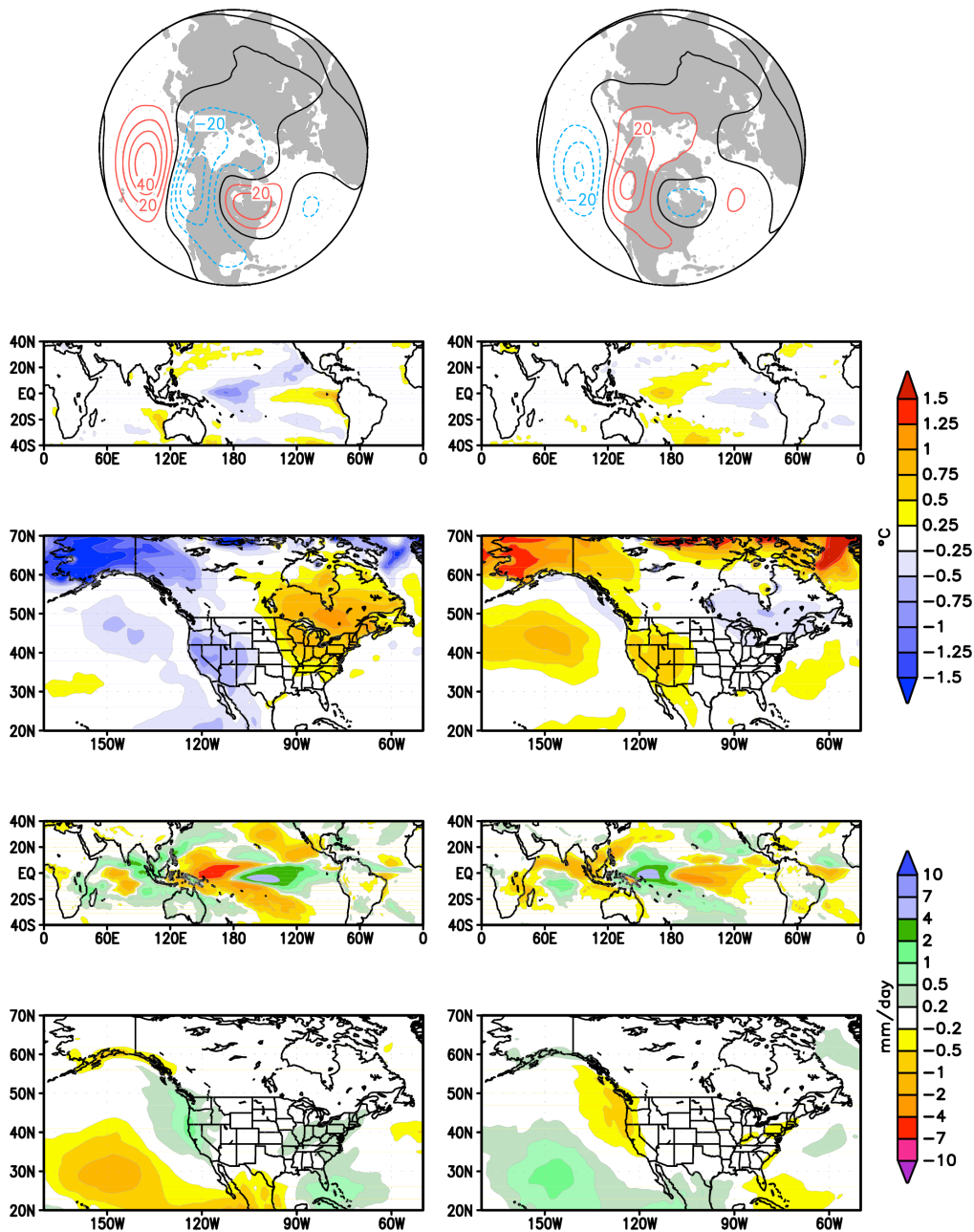
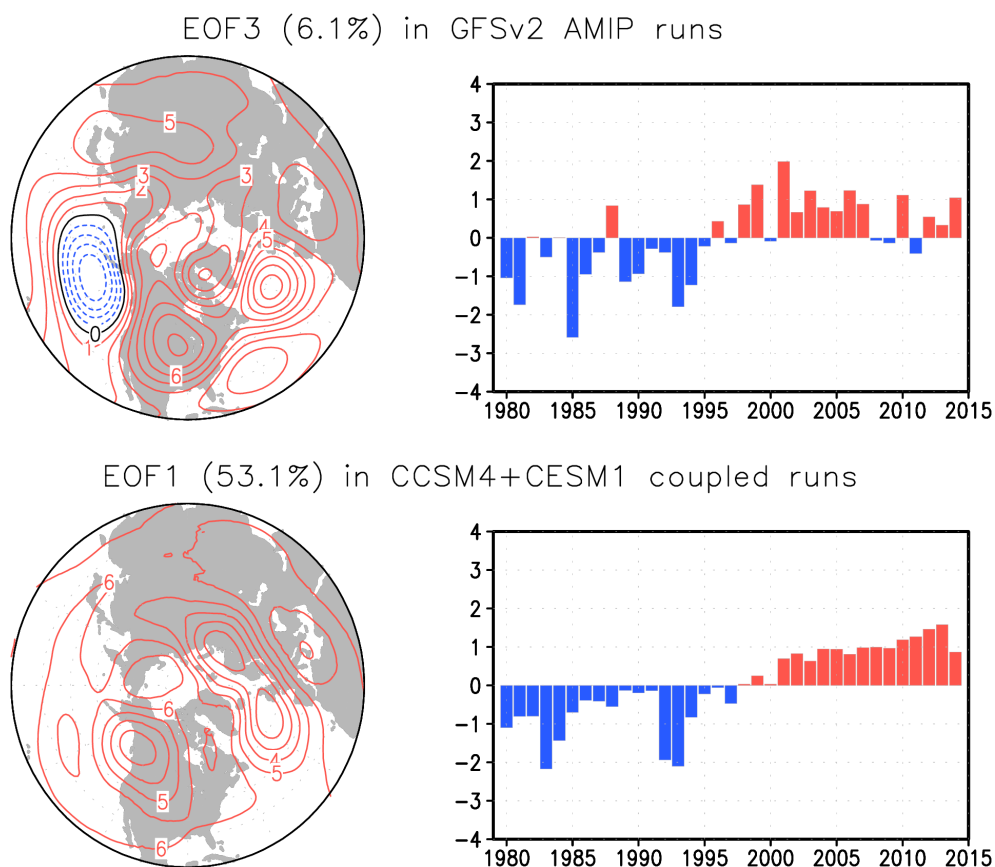


Figure 7. (left) The composite DJF anomalies of (first row) Northern Hemisphere 500-hPa height, (second row) tropical SST, (third row) North American surface temperature, (fourth row) tropical precipitation, and (fifth row) North American precipitation for 7 strongest cases with positive PC2 values from GFSv2 simulations shown in Figure 4. (right) Corresponding anomalies for 7 strongest cases with negative PC2 values shown in Figure 4. The contour interval of height fields in the first row is 10 meter.

1211



1212  
1213  
1214  
1215  
1216  
1217  
1218  
1219  
1220  
1221  
1222  
1223  
1224  
1225  
1226  
1227  
1228  
1229  
1230  
1231  
1232  
1233  
1234

Figure 8. Top panels show (left) the spatial pattern and (right) standardized PC time series of EOF3 of GFSv2 simulated 50-member ensemble mean winter (DJF) season 500-hPa heights. The bottom panels show (left) the spatial pattern and (right) standardized PC time series of the leading EOF of 50-member ensemble mean winter (DJF) season 500-hPa heights in coupled model runs which include 20 runs from CCSM4 and 30 runs from CESM1. The analysis is computed over the 20°N-90°N domain for 1979/80 through 2013/14. The EOF patterns are shown as the regressions of the heights onto the standardized PC time series, and drawn at the interval of 1 meter for a 1 standardized departure of PC index.

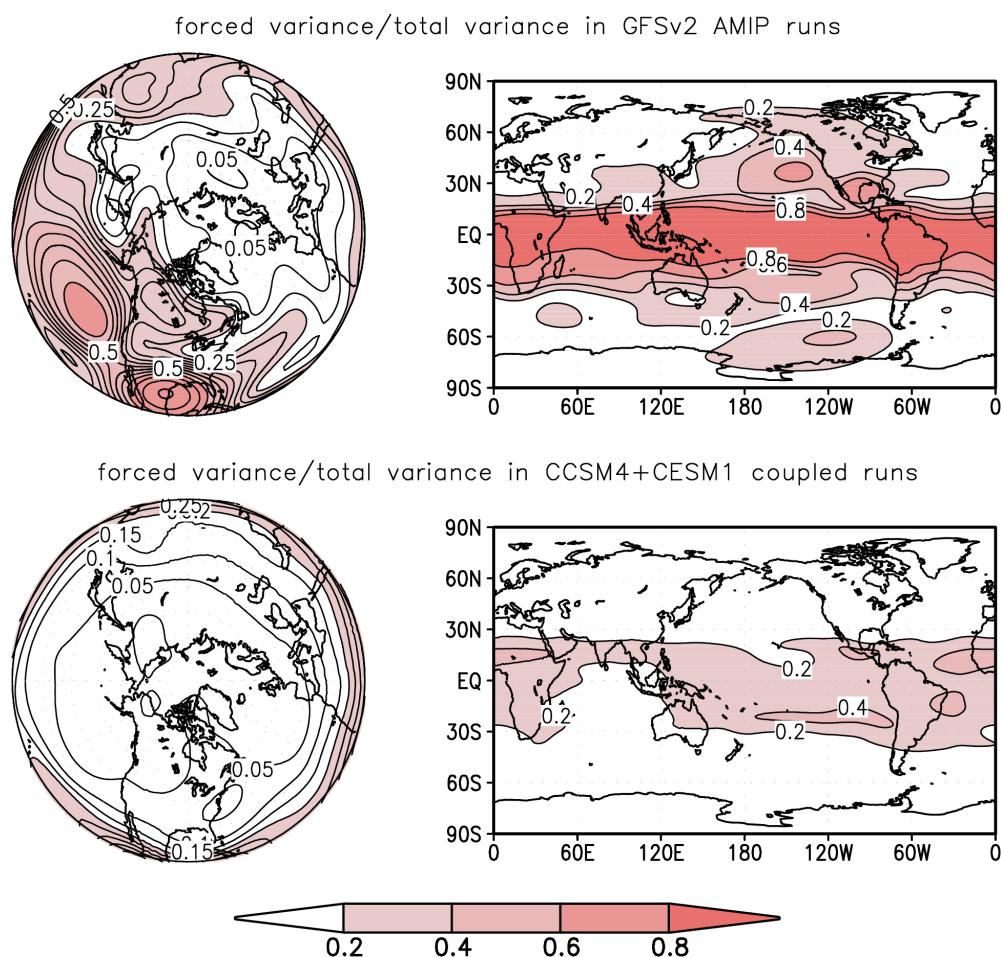
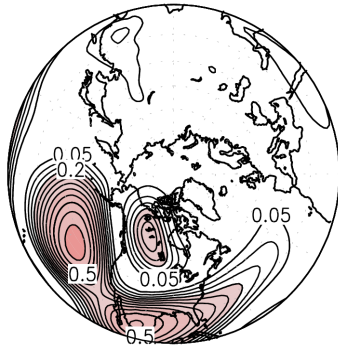


Figure 9. (Top) The ratio of forced component to the total variance of winter (DJF) seasonally averaged 500-hPa height for 1979/80 through 2013/14 in GFSv2 AMIP runs. The results are shown for (left) the NH polar cap to 20°N, and for (right) the global domain. (Bottom) corresponding results from coupled model runs which are the combinations of the runs from CCSM4 and CESM1. The contour interval is 0.05 for left panels and 0.2 for right panels. Forced variability is computed from the variance of ensemble means. Total variability is computed from the concatenated time series of the individual members. For two coupled models, the total variability is computed for each separately, and then averaged.

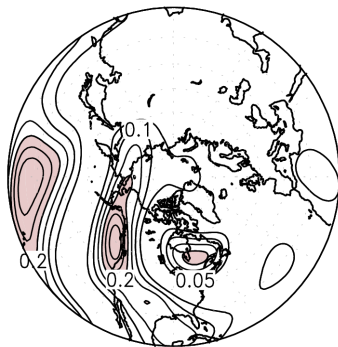


1257

forced EOF1 variance/total variance



forced EOF2 variance/total variance



forced EOF3 variance/total variance



1258

1259

1260

1261

1262

1263

1264

1265

1266

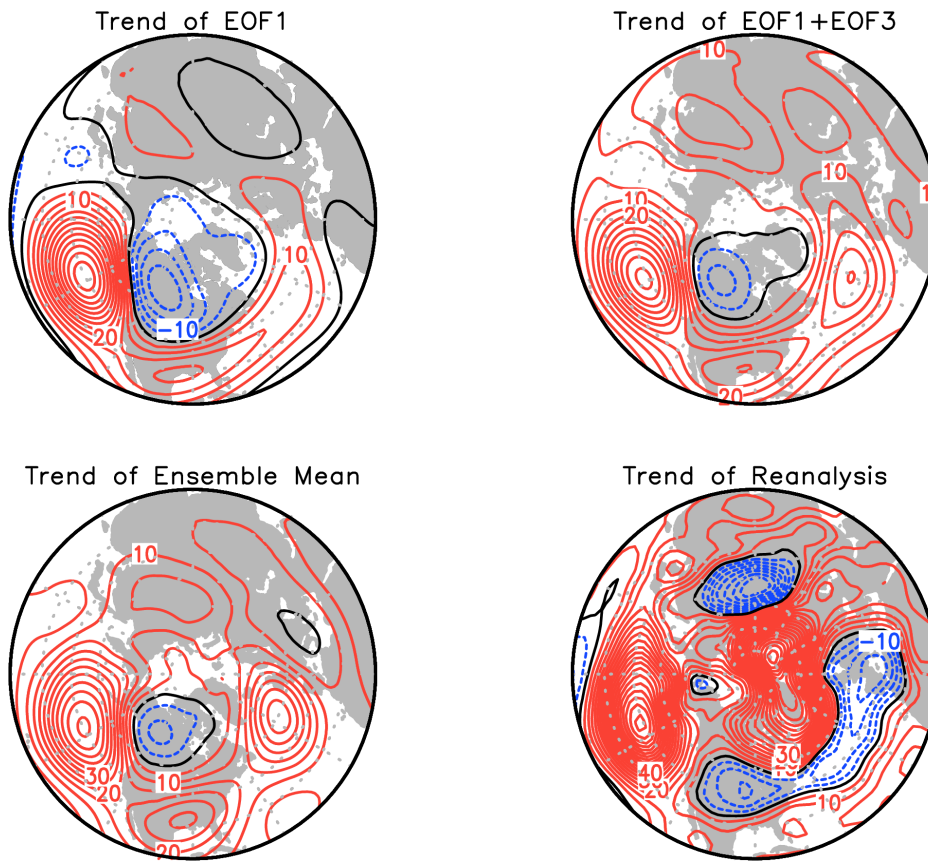
1267

1268

1269

Figure 10. The ratio of the leading three EOFs of forced component to the total variance of winter (DJF) seasonally averaged 500-hPa height for 1979/80 through 2013/14 in GFSv2 AMIP runs. The height anomalies projecting on different modes can be computed as the scalar product of different EOF patterns and the associated PC time series. The contour interval is 0.05.

1270



1271  
1272  
1273  
1274  
1275  
1276  
1277  
1278  
1279  
1280  
1281  
1282  
1283  
1284  
1285  
1286  
1287  
1288

Figure 11. The trend pattern of EOF1, the sum of EOF1 and EOF3, and the trend pattern of ensemble mean of winter (DJF) season 500-hPa heights from GFSv2 AMIP runs over the 20°N-90°N domain for 1979/80 through 2013/14. The observed trend pattern is shown in lower right. The trend patterns of EOF1 and EOF3 are obtained by the product between the EOF pattern and the total trend of the corresponding PC time series (the total trend is -1.09 standardized unit for PC1 and 2.0 standardized unit for PC3) shown in the top panels of Figure 1 and Figure 8, respectively. The contour interval is 5 meter.



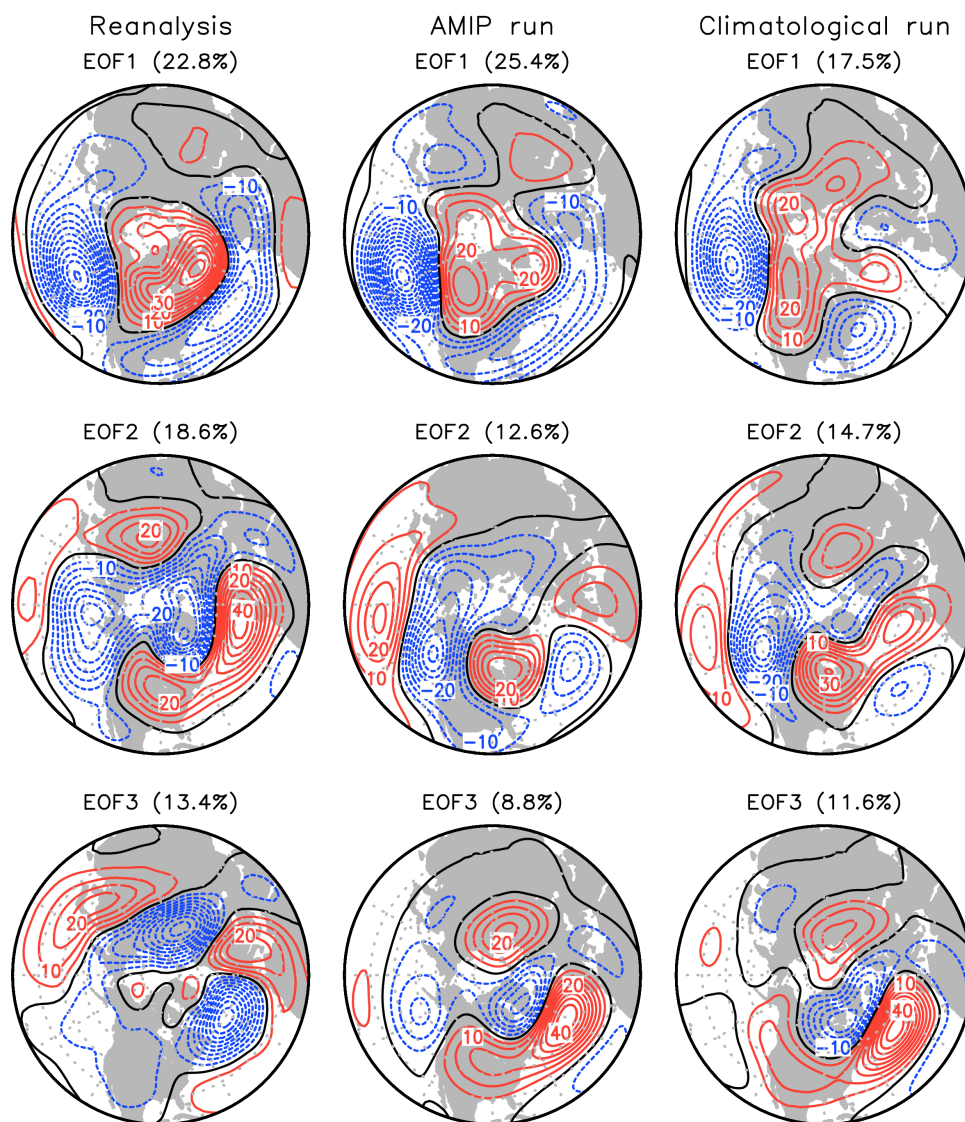


Figure A1. The spatial pattern of the leading three EOFs of winter (DJF) season 500-hPa heights from (left) observations, (middle) the concatenation of all 50 AMIP runs of GFSv2 and (right) a 100-yr-long GFSv2 climatological run in which the model is driven by observed SST climatology. Note that the model data used here are not ensemble means. The observational estimate is based on NCEP reanalysis for 1979/80 through 2013/14. The analysis is computed over the 20°N-90°N domain. The EOF patterns are shown as the regressions of the heights onto the standardized PC time series, and drawn at the interval of 5 meter for a 1 standardized departure of PC index.

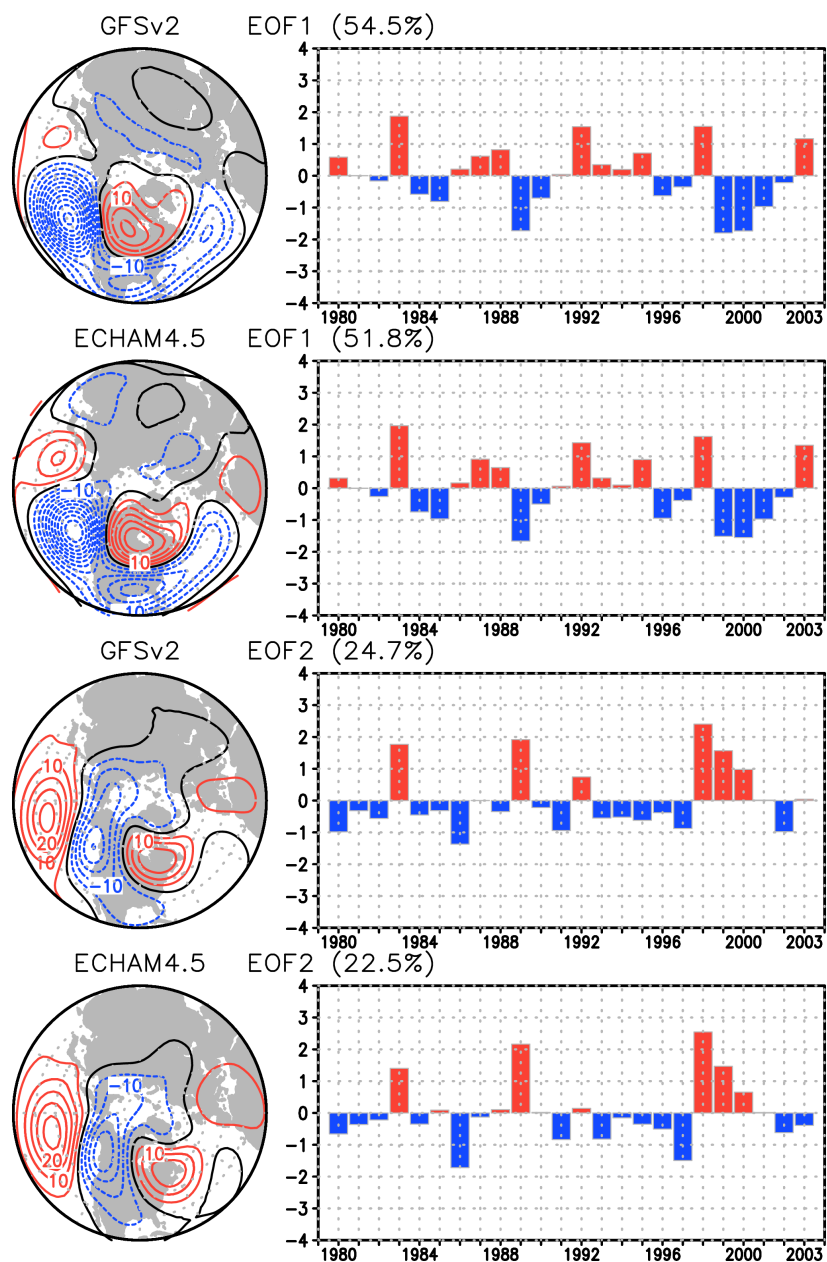


Figure B1. (left) The spatial pattern and (right) standardized PC time series of the leading two EOFs of winter (DJF) season 500-hPa ensemble mean heights from GFSv2 AMIP runs and ECHAM4.5 AMIP runs for the common period of 1979-2003. The analysis is computed over the 20°N-90°N domain based on 50-member ensemble mean from GFSv2 model and 85-member ensemble mean from ECHAM4.5 model. The EOF patterns are shown as the regressions of the heights onto the standardized PC time series, and drawn at the interval of 5 meter for a 1 standardized departure of PC index.

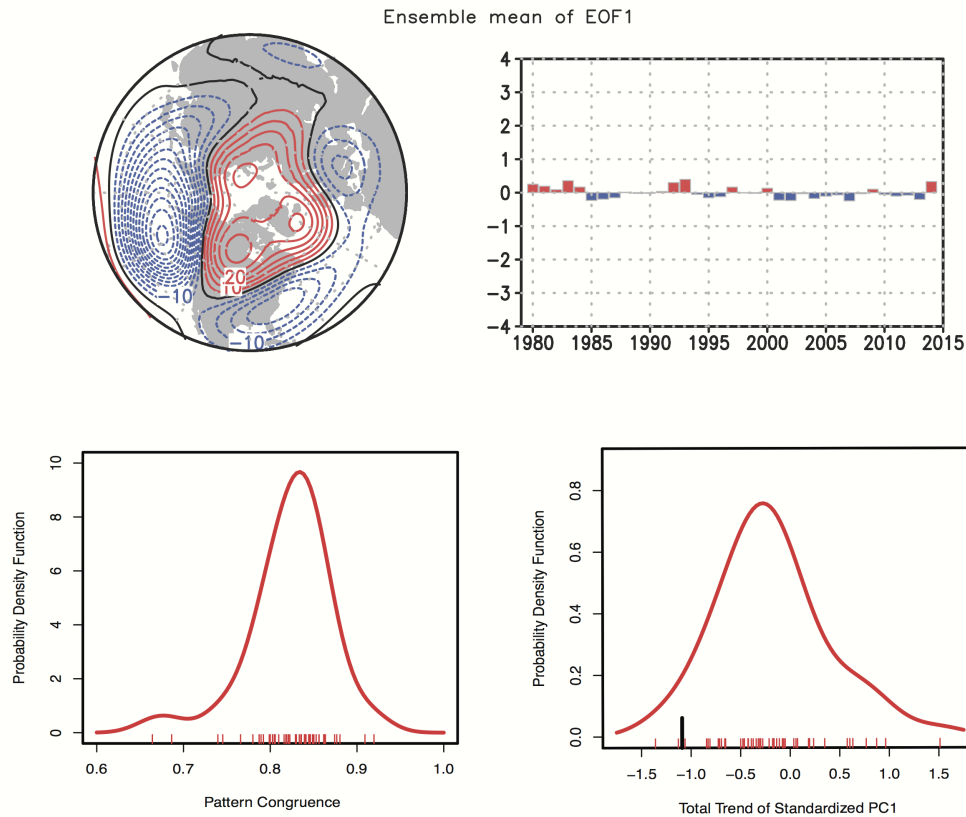


Figure C1. Ensemble mean of (top left) the spatial pattern and (top right) standardized PC time series of the leading EOF of winter (DJF) season 500-hPa heights averaged over 50 individual coupled runs which include 20 runs from CCSM4 and 30 runs from CESM1. (bottom left) Probability distribution function (PDF) for the EOF1 pattern congruence between individual coupled runs (indicated by short red lines) and NCEP reanalysis shown in Figure A1. (bottom right) PDF for 1979-2014 trend of standardized PC time series of the leading EOF (PC1) from the individual coupled model samples (indicated by short red lines), and the value of ensemble mean forced trend of PC1 in the AMIP simulations is also shown (indicated by long black line). Abscissa is of the total change during 1979-2014. The EOF analysis is computed over the 20°N-90°N domain for 1979/80 through 2013/14 and pattern congruence analysis is computed over the same domain. The EOF patterns are shown as the regressions of the heights onto the standardized PC time series, and drawn at the interval of 5 meter for a 1 standardized departure of PC index. The PDF is a nonparametric curve constructed using the R software program, which utilizes a kernel density estimation and a Gaussian smoother.